Constraining galaxy overdensities around three z ~ 6.5 quasars with ALMA and MUSE

Meyer, R.A.; Decarli, R.; Walter, F.; Li, Q.; Wang, R.; Mazzucchelli, C.; ... ; Venemans, B.P.

The Astrophysical Journal, 927:141 (22pp), 2022 March 10 https://doi.org/10.3847/1538-4357/ac4f67

Constraining Galaxy Overdensities around Three $z \sim 6.5$ Quasars with ALMA and MUSE

Romain A. Meyer[1], Roberto Decarli[2], Fabian Walter[1], Qiong Li[3,4,5], Ran Wang[3,5], Chiara Mazzucchelli[6], Eduardo Bañados[1], Emanuele P. Farina[7], and Bram Venemans[8]
[1] Max Planck Institut für Astronomie, Königstuhl 17, D-69117, Heidelberg, Germany; meyer@mpia.de
[2] INAF—Osservatorio di Astrofisica e Scienza dello Spazio di Bologna, via Gobetti 93/3, I-40129, Bologna, Italy
[3] Department of Astronomy, School of Physics, Peking University, Beijing 100871, People's Republic of China
[4] Department of Astronomy, University of Michigan, 311 West Hall, 1085 S. University Ave, Ann Arbor, MI 48109-1107, USA
[5] Kavli Institute for Astronomy and Astrophysics, Peking University, Beijing, 100871, People's Republic of China
[6] European Southern Observatory, Alonso de Cordova 3107, Vitacura, Region Metropolitana, Chile
[7] Max Planck Institut fur Astrophysik, Karl-Schwarzschild-Strae 1, D-85748 Garching bei München, Germany
[8] Leiden Observatory, Leiden University, PO Box 9513, 2300 RA Leiden, The Netherlands
Received 2021 October 29; revised 2022 January 7; accepted 2022 January 24; published 2022 March 10

Abstract

We quantify galaxy overdensities around three high-redshift quasars with known $[\mathrm{C\,II}]_{158\,\mu\mathrm{m}}$ companions: PJ231–20 ($z = 6.59$), PJ308–21 ($z = 6.24$), and J0305–3150 ($z = 6.61$). Recent SCUBA2 imaging revealed the presence of 17 submillimeter galaxies (SMGs) with sky separations $0\farcm7 < \theta < 2\farcm4$ from these three quasars. We present ALMA Band 6 follow-up observations of these SCUBA2-selected SMGs to confirm their nature and redshift. We also search for continuum-undetected $[\mathrm{C\,II}]_{158\,\mu\mathrm{m}}$ emitters in the ALMA pointings and make use of archival MUSE observations to search for Lyα emitters (LAEs) associated with the quasars. While most of the SCUBA2-selected sources are detected with ALMA in the continuum, no $[\mathrm{C\,II}]_{158\,\mu\mathrm{m}}$ line emission could be detected, indicating that they are not at the quasar redshifts. Based on the serendipitous detection of CO 7–6 and $[\mathrm{C\,I}]_{809\,\mu\mathrm{m}}$ emission lines, we find that four SMGs in the field of PJ231–20 are at $z \sim 2.4$, which is coincident with the redshift of an Mg II absorber in the quasar rest-frame UV spectrum. We report the discovery of two LAEs within <0.6 cMpc of PJ231–20 at the same redshift, indicating an LAE overdensity around this quasar. Taken together, these observations provide new constraints on the large-scale excess of Lyα- and $[\mathrm{C\,II}]_{158\,\mu\mathrm{m}}$-emitting galaxies around $z > 6$ quasars and suggest that only wide-field observations, such as MUSE, ALMA, or JWST mosaics, can reveal a comprehensive picture of large-scale structure around quasars in the first billion years of the universe.

Unified Astronomy Thesaurus concepts: Quasars (1319); Quasar-galaxy pairs (1316); High-redshift galaxies (734); Lyman-alpha galaxies (978); Submillimeter astronomy (1647)

1. Introduction

Observations of $z > 6$ quasars show that they are powered by supermassive black holes (SMBHs) as massive as $10^9\,M_\odot$ (e.g., De Rosa et al. 2011, 2014; Mazzucchelli et al. 2017b; Bañados et al. 2018; Yang et al. 2020; Wang et al. 2021). Their surprisingly high masses, accumulated within less than a Gyr since the big bang, are a puzzle for galaxy evolution and black hole growth theories. One formation pathway is through the existence of massive seed black holes ($\gtrsim 10^3\,M_\odot$) at $z \sim 15$–30 created by the collapse of massive gas clouds (e.g., Oh & Haiman 2002; Bromm & Loeb 2003; Begelman et al. 2006; Ferrara et al. 2014; Inayoshi & Haiman 2014), that of Population III stars (e.g., Bond et al. 1984; Madau et al. 2001; Latif et al. 2013; Valiante et al. 2016), or the runaway collision of stars in compact clusters (e.g., Omukai et al. 2008; Devecchi & Volonteri 2009; Katz et al. 2015; Sakurai et al. 2017). Radiatively inefficient accretion, close to or even above the Eddington limit, is another possible scenario explaining the presence of SMBHs with masses of $\sim 10^9\,M_\odot$ already at $z \sim 6$. Such extreme accretion histories are thought to be made possible by an abundance of gas-rich mergers or the presence of SMBH seeds in massive metal-poor gas halos (e.g., Hopkins et al. 2008; Narayanan et al. 2008; Overzier et al. 2009; Angulo et al. 2012; Latif & Volonteri 2015; Habouzit et al. 2019; Wise et al. 2019). Either way, most models of black hole formation and growth postulate or find that luminous $z > 6$ quasars should reside in the densest environments and effectively trace the emergence of the first large-scale structures in the universe (see, e.g., Haiman & Quataert 2004; Overzier et al. 2009; Volonteri 2010; Latif & Ferrara 2016; Inayoshi et al. 2020, for comprehensive reviews).

A direct prediction of this hypothesis is the presence of galaxy overdensities around quasars in the first billion years. Since the first discoveries, more than 200 quasars at $z > 6$ have been detected (e.g., Fan et al. 2001, 2004, 2006; Venemans et al. 2007; Mortlock et al. 2011; Carnall et al. 2015; Reed et al. 2015; Venemans et al. 2015; Bañados et al. 2016; Jiang et al. 2016; Reed et al. 2017; Bañados et al. 2018; Wang et al. 2018; Yang et al. 2019; Wang et al. 2021). This large sample of early luminous quasars has enabled the possibility to probe their supposedly overdense environment. However, despite long and sustained efforts with optical/IR ground- and space-based observatories, evidence for galaxy overdensities around these objects is mixed and contradictory (e.g., Willott et al. 2005; Ajiki et al. 2006; Kim et al. 2009; Utsumi et al. 2010; Bañados et al. 2013; Simpson et al. 2014; Mazzucchelli et al. 2017a;

Farina et al. 2017; Goto et al. 2017; Champagne et al. 2018; Mignoli et al. 2020; Miller et al. 2020). Although most $z > 6$ quasar fields have not been searched systematically and uniformly for overdensities, the current absence of clear evidence of galaxy overdensities around $z > 6$ quasars is an outstanding challenge to our current paradigm of black hole growth and galaxy evolution.

Recently, ALMA and NOEMA observations of the [C II]$_{158\,\mu m}$ line in high-redshift quasars have revealed the presence of close (<60 proper kpc, $<1000\,km\,s^{-1}$) [C II]$_{158\,\mu m}$-bright companions found around ∼30% of luminous $z \sim 6$ quasars (Decarli et al. 2017; Willott et al. 2017; Decarli et al. 2018, 2019; Neeleman et al. 2019; Venemans et al. 2020). These objects tantalizingly hint at the long-predicted large-scale overdensity around early quasars, but the limited field of view of ALMA only constrains the smaller scales (<1 comoving Mpc) of the galaxy−quasar correlation at $z > 6$. Alternatively, it is possible that these companion galaxies could simply be in the process of merging with the quasar (e.g., Decarli et al. 2019; Neeleman et al. 2019), as is expected if SMBH growth is driven by mergers (e.g., Hopkins et al. 2008). Therefore, the overabundance of companions on small scales might not necessarily trace larger overdensities, but rather result from a selection bias toward ongoing or recent mergers (which fuel the SMBH gas accretion and increase its likelihood of being detected as a hyperluminous quasar). Constraining the large-scale cross-correlation of galaxies and quasars at $z > 6$ is thus necessary to distinguish these two competing hypotheses.

In this paper, we investigate the large-scale environment of three $z > 6$ quasars with known bright [C II]$_{158\,\mu m}$ companions: J0305–3150 (Venemans et al. 2019), PJ231–20, and PJ308–21 (Decarli et al. 2017). J0305–3150, PJ231–20, and PJ308–21 have SMBH masses of $2.00^{+0.22}_{-0.64} \times 10^9\,M_\odot$, $1.89^{+0.34}_{-0.45} \times 10^9\,M_\odot$, and $1.69^{+0.20}_{-0.35} \times 10^9\,M_\odot$, respectively (Mazzucchelli et al. 2017b; Neeleman et al. 2021; E. Farina et al. 2022 in preparation). These quasars were observed with the Submillimeter Common-User Bolometer Array-2 (SCUBA2) on the James Clerk Maxwell Telescope (Holland et al. 2013) at 850 and 450 μm as part of a larger survey of quasar environments described in Li et al. (2020b) and Q. Li et al. (2022, in preparation). The SCUBA2 images revealed numerous submillimeter galaxies (SMGs) detected at $0.7 \lesssim \theta \lesssim 2\farcm4$ from each quasar (corresponding to ∼1.8–5.8 comoving Mpc at the quasar redshifts). To test the possibility that these SMGs could be part of a large-scale overdensity associated with the $z > 6$ quasars, we have observed the 17 brightest with ALMA to confirm their redshift. The spectral tunings were placed such that the [C II]$_{158\,\mu m}$ line would fall in the upper sideband if the SMGs were at the quasar redshift. Moreover, we also make use of archival MUSE observations of the quasars to probe potential overdensities of LAEs on smaller scales ($\lesssim$2 comoving Mpc) than the SMG ALMA pointings (∼1.8–5.8 comoving Mpc). This paper thus aims to present a comprehensive analysis of the galaxy under/overdensity around three $z > 6$ quasars probed by SCUBA2, ALMA, and MUSE.

The structure of the paper is as follows. In Section 2, we describe our ALMA observations of the selected SCUBA2 SMGs in three high-redshift quasar fields. We present in Section 3 the continuum sources detected with ALMA and discuss the ALMA and SCUBA2 continuum fluxes. We assess the redshift of the detected continuum sources using emission lines and photometric redshifts and capitalizing on ancillary HST and Spitzer imaging combined with the ALMA and SCUBA2 measurements. In Section 4, we present the results of a search for serendipitous [C II]$_{158\,\mu m}$ line emitters (undetected in the continuum) in the ALMA pointings. We present in Section 5 the LAEs found in the archival MUSE observations of our three quasars. We present our updated constraints on the overdensity and the nature of galaxies around high-redshift quasars in Section 6 before concluding in Section 7.

Throughout this paper, we assume a concordance cosmology with $H_0 = 70\,km\,s^{-1}\,Mpc^{-1}$, $\Omega_M = 0.3$, $\Omega_\Lambda = 0.7$. All magnitudes are given in the AB system (Oke & Gunn 1983). At the redshift of the quasars ($z \sim 6.5$), 1″ corresponds to 5.46 proper kpc.

2. Observations and Data Reduction

2.1. Quasar Fields Studied in This Work and Existing Archival Data

This work focuses on three $z > 6$ quasars: J0305–3150, PJ231–20, and PJ308–21. J0305–3150 was originally discovered in the VISTA Kilo-Degree Infrared Galaxy (VIKING) Survey (Venemans et al. 2013), while PJ308–21 (Bañados et al. 2016) and PJ231–20 (Mazzucchelli et al. 2017b) were discovered in the Panoramic Survey Telescope and Rapid Response System (PAN-STARRS) quasar surveys. All three quasars were observed with ALMA to detect the redshifted [C II]$_{158\,\mu m}$ emission line, obtaining, among other properties, precise redshifts: $z_{J0305-3150} = 6.6145 \pm 0.0001$ (Venemans et al. 2016), $z_{PJ231-20} = 6.58651 \pm 0.00017$, and $z_{PJ308-21} = 6.2342 \pm 0.0010$ (Decarli et al. 2017). The [C II]$_{158\,\mu m}$ observations also revealed the presence of companions bright in [C II]$_{158\,\mu m}$ and in the dust continuum emission (e.g., Decarli et al. 2017; Neeleman et al. 2019; Venemans et al. 2020). Further ALMA and MUSE observations uncovered three close (<40 kpc) [C II]$_{158\,\mu m}$ emitters (Venemans et al. 2019), as well as a nearby Lyα emitter (Farina et al. 2017), in the vicinity of J0305–3150. These studies suggest that these three quasars could trace particularly overdense environments.

2.2. ALMA Observations of Submillimeter SCUBA2 Sources

The three quasar fields have been observed with SCUBA2 as part of a larger submillimeter survey of $z \sim 6$ quasars to study their environments (Li et al. 2020b; Q. Li et al. 2022, in preparation). In order to study the possible large-scale overdensities around the three $z \sim 6.5$ quasars, we have selected $>3.5\sigma$ ($\gtrsim$4 mJy) SMGs in their vicinity ($0\farcm7 \lesssim \theta \lesssim 2\farcm4$) based on the SCUBA2 850 μm maps. No cutoff was imposed on the maximum distance of SMGs from the quasar, which simply results from the SCUBA2 field of view and the depth of the data. The resulting sample contains four SCUBA2-selected SMGs around both J0305 and PJ231 and nine around PJ308, for a total of 17. The reduction and analysis of the SCUBA2 data are detailed extensively in Li et al. (2020b; see also Q. Li et al. 2022, in preparation, for the SMG results), to which we direct the interested reader. We reproduce in Appendix A the SCUBA2 imaging to make this paper self-contained.

The SCUBA2 sources were each observed in Band 6 for ≃10 minutes on source with a single ALMA pointing (program 2019.1.01003.S, PI: R. Decarli). The spectral setup was chosen such that the center of the upper sideband was at the redshifted frequency of [C II]$_{158\,\mu m}$ of the central quasar (∼250–270 GHz). The array configuration was chosen to have a relatively low spatial resolution between 0″.7 and 1″.4, as the aim is to detect the

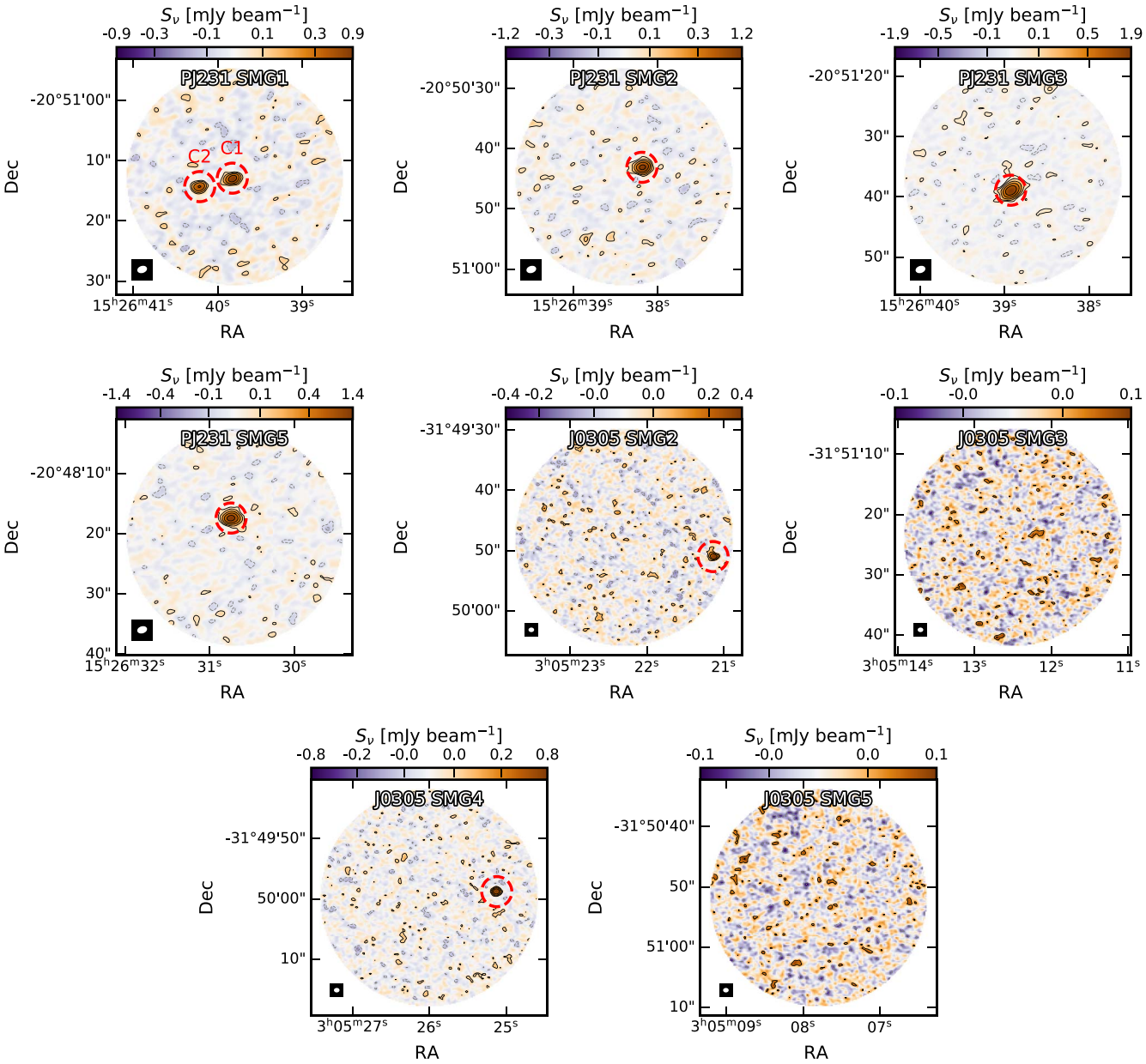

Figure 1. ALMA continuum imaging of the SCUBA2-identified SMGs in the fields around PJ231–20 and J0305–3150. The color scaling is log-linear for better contrast, and the contours are logarithmic: $(-2, 2, 4, 8, 16, 32)\sigma$, where σ is the rms noise (see Table 1). The identified continuum sources ($>5\sigma$) are enclosed by dashed red circles and are labeled "C1" and "C2" if multiple sources are detected in the same pointing. The beam is plotted in the lower left corner (white against black square), and the sizes are tabulated in Table 1. The ALMA detections can be offset from the center of the pointing owing to the large beam of the SCUBA2 imaging (13″ at 850 μm, e.g., of the order of the ALMA field of view) from which the target was selected.

[C II]$_{158\ \mu m}$ line in the SMGs and thus try to confirm whether they are at the quasar redshift.

Imaging and cleaning were performed with CASA, and the final images and data cubes were produced in the following fashion. First, the visibilities were imaged with a natural weighting and cleaned down to 2σ (rms noise) to produce preliminary continuum maps and data cubes. Continuum sources (peak surface brightness $>5\sigma$) were identified in most SMG pointings (see Figures 1 and 2). Preliminary spectra of the continuum sources were then extracted using an $r = 2''$ aperture and fitted with a simple Gaussian profile and a constant continuum to identify prominent lines (if any). Frequencies at ± 1.25 times the FWHM of significant lines were subsequently masked to image line-free continuum maps and cubes from the visibilities. The line-free continuum was then subtracted in the u-v plane to produce continuum-subtracted cubes with 50 km s^{-1} channels (this step was only performed in pointings where continuum sources were detected). The continuum-subtracted cubes were then imaged and cleaned down to 2σ (rms) with circular masks on the identified continuum sources. We present in Table 1 the beam size, continuum rms, and sensitivity per channel and per beam of the cleaned data products for each quasar field.

3. Continuum-detected Sources

3.1. ALMA Continuum Detections

We present the continuum maps of the 17 ALMA pointings on SMGs detected in SCUBA2 850 μm images in Figures 1 and 2. In 12 out of 17 pointings, we detect a continuum source in the ALMA data, and in 3 of those, we even detect

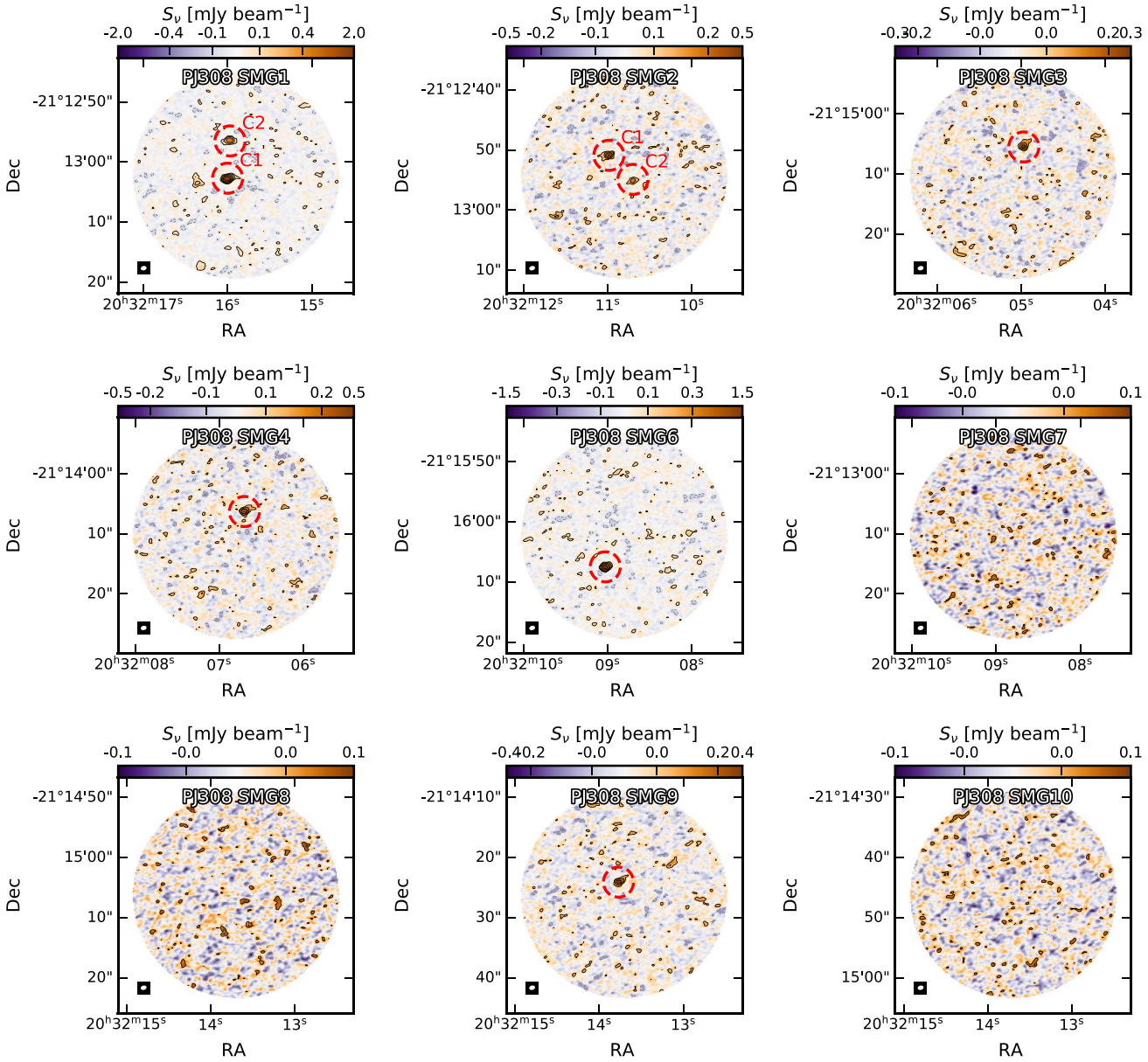

Figure 2. Same as Figure 1, but for PJ308–21.

Table 1
Summary of Our ALMA Observations of SMGs in the Fields of Three $z > 6.5$ Quasars

Quasar	$N_{\rm SMGs}$	Continuum rms (mJy beam^{-1})	Beam (arcsec^2)	rms per Channel[a] (mJy beam^{-1})	$\nu_{\rm obs}$ (GHz)
PJ231–20	4	3.0×10^{-2}	$1\farcs66 \times 1\farcs17$	0.55/0.61	234.95 – 238.62 / 248.70 – 252.35
J0305–3150	4	2.5×10^{-2}	$0\farcs93 \times 0\farcs75$	0.44/0.49	234.08 – 237.74 / 247.77 – 251.40
PJ308–20	9	3.2×10^{-2}	$0\farcs98 \times 0\farcs72$	0.57/0.61	246.45 – 250.18 / 260.85 – 264.58

Notes. We report the beam size and rms of the continuum images, as well as the sensitivity and frequency coverage of the data cubes.
[a] The rms per channel is given for 50 km s^{-1} channels and for both sidebands.

two sources. Each source is given a unique identifier consisting of the quasar name, SMG number in the original SCUBA2 catalog, and source name ("C1" or "C2" for continuum sources, where "C1" is the brightest continuum source in the ALMA pointing and "C2" is the fainter, secondary source in multiple systems).

The continuum fluxes were extracted using an $r = 2''$ aperture, which encompasses all of the 2σ emission for the vast majority of sources (a large fraction of the SCUBA SMGs are resolved in a few beams in the ALMA continuum maps). The fluxes were computed using the residual scaling method (e.g., Jorsater & van Moorsel 1995; Walter & Brinks 1999; Walter et al. 2008;

Table 2
Properties of the Detected Continuum Sources

ID	R.A.	Decl.	SN_{Cont}	S_ν (mJy)	SN_{Line}	ν_{Line} (GHz)	$S_\nu\Delta v$ (Jy km s^{-1})	FWHM (km s^{-1})
PJ231-SMG1-C1	15:26:39.83	−20:51:12.87	29.9	1.09 ± 0.08	5.2	237.27 ± 0.20	1.85 ± 0.63	1960[a]
PJ231-SMG1-C2	15:26:40.22	−20:51:14.28	19.8	0.74 ± 0.08	⋯	⋯	⋯	⋯
PJ231-SMG2-C1	15:26:38.19	−20:50:43.08	41.2	1.52 ± 0.07	5.8	236.01 ± 0.03	0.47 ± 0.11	291
PJ231-SMG3-C1	15:26:38.93	−20:51:38.89	60.6	2.94 ± 0.08	9.6	235.40 ± 0.10	2.16 ± 0.40	1167[a]
PJ231-SMG5-C1	15:26:30.75	−20:48:17.40	45.4	1.84 ± 0.08	8.9	236.92 ± 0.08	1.84 ± 0.31	1270[a]
J0305-SMG2-C1	03:05:21.14	−31:49:51.02	15.7	0.53 ± 0.07	⋯	⋯	⋯	⋯
J0305-SMG4-C1	03:05:25.12	−31:49:58.82	31.3	0.74 ± 0.07	⋯	⋯	⋯	⋯
PJ308-SMG1-C1	20:32:16.00	−21:13:02.69	58.3	2.40 ± 0.11	4.3	262.54 ± 0.02	0.27 ± 0.08	129
PJ308-SMG1-C2	20:32:15.97	−21:12:56.49	13.9	0.82 ± 0.22	⋯	⋯	⋯	⋯
PJ308-SMG2-C1	20:32:10.99	−21:12:50.89	16.6	0.67 ± 0.10	⋯	⋯	⋯	⋯
PJ308-SMG2-C2	20:32:10.70	−21:12:54.88	5.42	0.92 ± 0.38	⋯	⋯	⋯	⋯
PJ308-SMG3-C1	20:32:04.97	−21:15:05.49	10.7	0.44 ± 0.09	⋯	⋯	⋯	⋯
PJ308-SMG4-C1	20:32:06.70	−21:14:06.30	15.1	0.65 ± 0.09	⋯	⋯	⋯	⋯
PJ308-SMG6-C1	20:32:09.03	−21:16:07.48	46.1	1.54 ± 0.10	⋯	⋯	⋯	⋯
PJ308-SMG9-C1	20:32:13.77	−21:14:24.09	11.4	0.43 ± 0.09	3.1	263.11 ± 0.02	0.081 ± 0.067	298

Notes. Flux densities are computed by taking the integrated flux in an aperture of $r = 2''$ and applying residual scaling (e.g., Jorsater & van Moorsel 1995; Walter & Brinks 1999; Walter et al. 2008; Novak et al. 2019). The line fluxes are rescaled by $1/0.84$ because the continuum-subtracted (in the u-v plane) data are averaged over $1.2 \times$ FWHM, which contain 84% of the flux for a Gaussian line (see Novak et al. 2020, Appendix A).
[a] The quoted width is that of the best-fit single Gaussian profile. In Appendix B we discuss how these can be attributed to CO 7–6 and $[C\,I]_{809\ \mu m}$ at $z \simeq 2.4$.

Novak et al. 2019) and are listed alongside the coordinates and detection significance of each continuum source in Table 2.

3.2. ALMA/SCUBA2 Continuum Flux Density Comparison

Only 70% of the SMGs selected in the SCUBA2 imaging have a continuum detection in the ALMA data. We now investigate the different continuum fluxes at $\lambda = 850\,\mu$m (SCUBA2) and $\lambda \simeq 1.3$ mm (ALMA) to determine whether this is expected for sources at various redshifts.

In order to do so, we model the dust in the optically thin limit using a modified blackbody spectrum. We include the prescription of Da Cunha et al. (2013) to model the effect of cosmic microwave background (CMB) heating and correct for contrast against the CMB. The opacity is assumed to follow the best-fit relation and coefficients of Dunne et al. (2003), $\kappa_{\nu_{rest}} = \kappa_{\nu_0}(\nu_{rest}/\nu_0)^\beta$, with $\nu_0 = c/(125\ \mu m)$, where β is the power-law dust emissivity index. We assume a fiducial dust temperature $T = 30$ K and dust emissivity $\beta = 1.5$ following the common values found in $0.1 \lesssim z \lesssim 2.8$ (e.g., Hwang et al. 2010), or $T = 47$ K as commonly used for high-redshift quasars (e.g., Beelen et al. 2006; Venemans et al. 2020).

We account for flux deboosting by correcting the observed SCUBA2 fluxes by a mean flux boosting factor of 1.19 for sources at a signal-to-noise ratio (S/N) of 4 (Q. Li et al. 2022, in preparation), which is similar to the S/N of our sources in the SCUBA2 images. We take into account the impact of multiplicity on the observed ALMA fluxes. This phenomenon is well known from earlier ALMA follow-up of SMGs (Barger et al. 2012; Smolčić et al. 2012; Hodge et al. 2013): unresolved bright SMGs in single-dish observations are often resolved in interferometric observations and break into multiple sources. Consequently, the total flux might not be recovered, as some resolved sources are below the sensitivity of the ALMA data. The number of SMGs showing multiple counterparts in high-resolution millimeter observations (e.g., the observed multiplicity) varies from 16% to 45% (Barger et al. 2012; Smolčić et al. 2012; Hodge et al. 2013). These are only lower limits since secondary or tertiary sources in multiple systems might not be bright enough to be detected in the shallow ALMA observations. In this work, 3 of the 15 SMGs have two corresponding ALMA detections, implying an observed multiplicity of the SMGs of >20%. Following Hodge et al. (2013), we assume an intrinsic multiplicity of 50%. We further assume that when a source is resolved in multiple components, the strongest source accounts for 65% of the total flux following what is observed in our multiple detections (see Table 2), which is an upper limit considering that some sources will not be detected in the ALMA continuum maps.

We can now predict the expected continuum densities at ∼250 GHz from the observed SCUBA2 continuum flux densities. For simplicity, we consider only the brightest source detected with ALMA. We compare in Figure 3 the observed flux density ratios against the ones extrapolated from modified blackbody SEDs for various dust temperatures, source multiplicity, and redshift. We find that we cannot constrain the redshift of the SMGs using the available ALMA and SCUBA2 continuum fluxes, as the redshift has a minimal impact on the flux ratios compared to multiplicity, which is poorly constrained. The excess of faint ALMA counterparts to bright SCUBA2 detections suggests that a significant fraction of the 850 μm flux density comes from sources undetected in the higher-resolution ALMA observations. This hypothesis is in agreement with the conservative assumptions of multiplicity and fraction of flux in the brightest source made above. In conclusion, the ALMA continuum detections are broadly in line with measured flux densities in the SCUBA2 imaging, and we attribute any discrepancies to faint sources that are resolved and undetected in the ALMA observations.

3.3. SCUBA2/ALMA SMG Redshifts from Emission Lines

The main aim of our observations is to confirm whether the SCUBA2 SMGs are at the redshift of the $z > 6$ quasar in the field by detecting their redshifted $[C\,II]_{158\ \mu m}$ line. Therefore, spectra for each ALMA continuum source were extracted from the continuum-subtracted data cubes using an $r = 2''$ aperture and applying residual scaling. A single Gaussian was fitted to each spectrum to locate any significant emission feature. For each emission line detected, a velocity-integrated emission-line

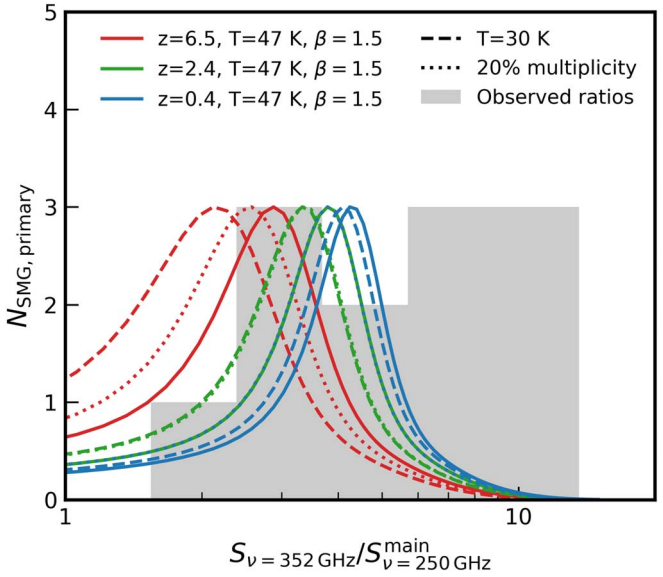

Figure 3. Observed continuum flux ratios (gray) between the SCUBA2 detections (352 GHz) and the primary ALMA counterpart (∼250 GHz). Predicted ratios based on modified blackbody SED models (see Section 3.2) are plotted for a dust temperature $T = 47$ K and dust emissivity index $\beta = 1.5$ at $z = 0.4$, 2.4, and 6.5 in blue, green, and red, respectively. Dashed and dotted lines indicate similar predictions with a lower temperature ($T = 30K$) or source multiplicity (20%). The excess of 352 GHz to 250 GHz flux is expected if our assumptions for the source multiplicity and fraction of flux in the brightest sources are conservative (see Section 3.2).

map was produced by integrating channels within $\pm 1.2 \times$ FWHM of the line. Additionally, control maps with the same velocity range, but containing the velocity channels adjacent to the lines, were produced to assess visually the significance of the line. These emission-line maps are presented in Figure 4.

We detect emission lines in six of the continuum-detected sources: four of the continuum sources in the field of PJ231–20 show $>5\sigma$ lines, and two of the sources around PJ308–21 have 3σ–4σ lines. Only the weak lines in PJ308-SMG1-C1 and PJ308-SMG9-C9 are approximately at the same redshift as that of the quasar, which we consider as marginal. Indeed, the emission lines of the PJ231 SMGs are detected in the lower sideband of the ALMA setup and can be ascribed to CO 7–6 and $[\mathrm{C\,I}]_{809\ \mu\mathrm{m}}$ at $z = 2.4$ coincident with the redshift of an Mg II absorber in the spectrum of the quasar (see Appendix B for a more detailed discussion of this result). All the detected line significances, FWHM, and frequencies are presented with the continuum source information in Table 2.

For the continuum sources without lines, we have stacked the spectrum at the rest-frame frequency of the $[\mathrm{C\,II}]_{158\ \mu\mathrm{m}}$ emission of the background quasar. The result is shown in Figure 5. We do not find evidence for $[\mathrm{C\,II}]_{158\ \mu\mathrm{m}}$ emission at the redshift of the quasar in the stacked spectrum.

The absence of lines close to the frequency of $[\mathrm{C\,II}]_{158\ \mu\mathrm{m}}$ at the redshift of the quasar cannot plausibly be attributed to a "weak" $[\mathrm{C\,II}]_{158\ \mu\mathrm{m}}$ line emission. At the mean continuum flux density (1.2 mJy) of the ALMA detections, the far-IR (FIR) luminosity (modeled as described above using a modified blackbody assuming standard dust parameters and $z = 6.5$) is $\sim 3.4 \times 10^{12}\ L_\odot$. The $[\mathrm{C\,II}]_{158\ \mu\mathrm{m}}$-to-FIR luminosity ratio in low-redshift ULIRGs and high-redshift quasars varies from 10^{-2} to 10^{-4} (Díaz-Santos et al. 2017; Novak et al. 2019; Li et al. 2020a; Pensabene et al. 2021). We would thus expect $[\mathrm{C\,II}]_{158\ \mu\mathrm{m}}$ lines in

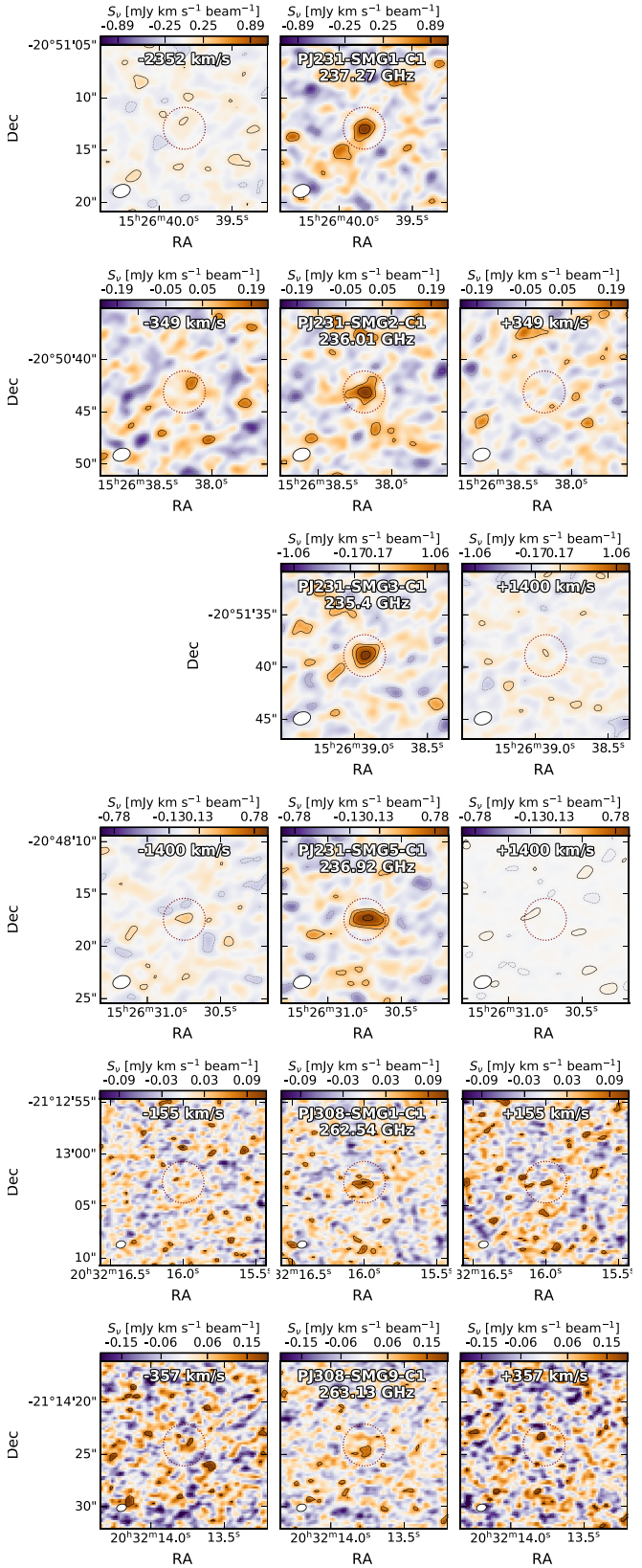

Figure 4. Emission-line map, velocity-integrated over $1.2 \times$ FWHM of the fitted Gaussian profile to the extracted spectrum. Each row features a significant emission line found in one of the ALMA continuum sources. For each line, we also provide two additional maps (left/right) integrated over the same velocity range but offset by ± 1.2FWHM. In two cases, either of these control maps is missing, as the emission is detected close to the edge of the band. The contours are logarithmic $(-4, -2, 2, 4, 8)\sigma$ (rms).

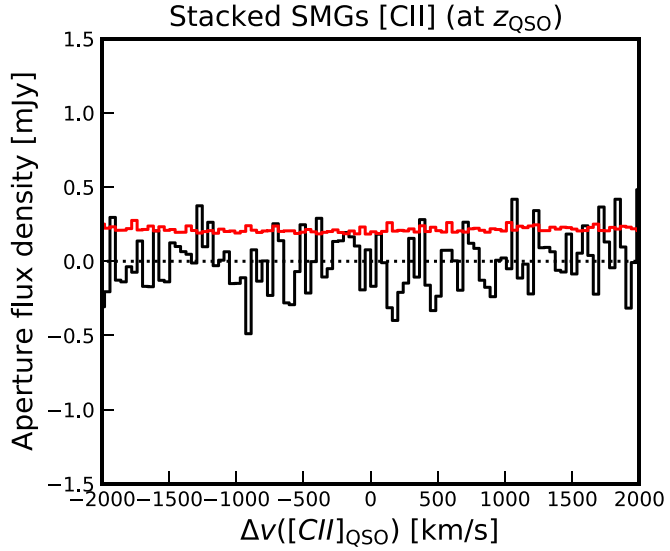

Figure 5. Stacked aperture-integrated ($r = 2''$) spectrum (black, error in red) of all ALMA continuum sources (with the exception of the $z = 2.4$ sources in the foreground of PJ231), centered at the redshifted frequency of the quasars' [C II]$_{158\ \mu m}$ emission line. The error array (red) is measured for each spectrum using the rms per beam rescaled to the number of beams in the $r = 2''$ aperture and subsequently stacked. We find no evidence of [C II]$_{158\ \mu m}$ emission in the stacked spectrum.

our sources with a luminosity $\sim 3.4 \times 10^8$–$10^{10}\ L_\odot$. Assuming a line width of 300 km s^{-1}, this is equivalent to a [C II]$_{158\ \mu m}$ line flux of 1–100 mJy over the full line width. With a sensitivity of $\sim$0.5 mJy per 50 km s^{-1} channel (see Table 1), the [C II]$_{158\ \mu m}$ lines should have been detected at least at the 4.4σ level in the sources with the strongest [C II]$_{158\ \mu m}$ deficit. In conclusion, the nondetection of [C II]$_{158\ \mu m}$ emission lines strongly suggests that the SMGs are not associated with the quasar and probably foreground sources.

3.4. SCUBA2/ALMA SMG Photometric Redshifts

In this section, we complement our analysis of the absence of [C II]$_{158\ \mu m}$ line detections in the SMGs targeted by studying their photometric redshifts. The three quasar fields of interest have ancillary HST/WFC3 F140W, and Spitzer/IRAC [3.6 μm] and [4.5 μm] imaging (see Table 3), which we can add to the SCUBA2 850 and 450 μm imaging (Q. Li et al. 2022, in preparation) and ALMA Band 6 observations presented in this work. Now that the positions of the SMGs are determined from the ALMA data, we can combine these data sets to constrain their spectral energy distribution (SED) and obtain reliable photometric redshifts using *MAGPHYS* (Da Cunha et al. 2015), a UV-to-FIR SED modeling code.

The HST images were reduced using the standard pipeline (see Decarli et al. 2019; Mazzucchelli et al. 2019, for more details). The photometry was extracted for all sources in the fields using *Sextractor* (Bertin & Arnouts 1996) using standard parameters[9] and *MAG_AUTO* magnitudes. We adopt the pipeline-reduced Spitzer images from Mazzucchelli et al. (2019), with a refined astrometric solution based on the Gaia DR1 catalog. Due to the spatial resolution of the data ($\sim 1\farcs2$–$1\farcs8$) and the limited sampling ($0\farcs6 \times 0\farcs6$), one of the sources (PJ308-SMG1-C1) is blended with foreground objects, and the photometry cannot be retrieved accurately using *Sextractor*. Therefore, we fit the blended SMG and the foreground objects simultaneously using the latest version of *Galfit* (Peng et al. 2002, 2010). We create a point-spread function (PSF) image by rescaling, interpolating, and upsampling images of $4 - 10$ (depending on the channel) stars in the field. Most sources are modeled with a single point-source profile, except the most extended ones with a Sérsic profile (which have the half-light radius and Sérsic index profiles n as additional parameters to the integrated magnitude and position). We show in Figure 6 the Spitzer imaging, the best-fit *Galfit* model, and the residuals. We check that the magnitude of the nearby unblended source (PJ308-SMG1-C2) measured with *Galfit* ($m_{CH1} = 19.28 \pm 0.03$, $m_{CH2} = 18.49 \pm 0.03$) is consistent with that measured by *Sextractor* ($m_{CH1} = 19.23 \pm 0.01$, $m_{CH2} = 18.49 \pm 0.17$). Table 4 lists the ancillary photometry and fluxes for all our continuum sources.

We fit the photometry of the ALMA continuum sources using *MAGPHYS-photoz* (Da Cunha et al. 2015; Battisti et al. 2019) and show the resulting posterior redshift distributions in Figure 7. The best-fit SEDs are presented in Appendix C. None of the continuum-detected sources have a photometric redshift consistent with that of the background quasar ($z > 6$). We conclude that the weak emission lines in PJ308-SMG1-C1 and PJ308-SMG9-C1 are either noise or low-redshift CO lines and that none of the SCUBA2-detected SMGs are likely to be at the background quasar redshift. The detection of $z \simeq 2.4$ CO 7–6 and [C I]$_{809\ \mu m}$ lines in the SMGs in the field of PJ231–20 supports this conclusion (see Appendix B), although the peak of the photometric redshift posterior is at $\sim$2 rather than $z \simeq 2.4$, a difference that could be explained by the low number of data points available to constrain the SEDs.

4. Searching for Serendipitous [C II]$_{158\ \mu m}$ Line Emitters

We have demonstrated in the previous section that the targeted SMGs are most likely foreground sources not associated with the background quasars. Nonetheless, [C II]$_{158\ \mu m}$ emitting sources without a detection in the ALMA continuum maps could also be associated with the background quasar. We thus set out to search for line emitters (e.g., without continuum emission) to constrain the large-scale structure around the three quasars studied here. In order to do so, we make use of two line-finding algorithms developed for interferometric data.

The first algorithm is *FindClumps* (Walter et al. 2016; Decarli et al. 2019). *FindClumps* convolves the imaged and cleaned datacube with boxcar filters of a given width in the spectra direction (e.g., it effectively slices and averages a number of continuous channels) to produce a velocity-integrated line map, which is then passed through *Sextractor* (Bertin & Arnouts 1996) to find significant sources. The operation is repeated for different boxcar widths (in this case 3 to 19 channels of 50 km s^{-1}), after which the sources are grouped together (sky separation in frequency between two emission features (here 0.1 GHz). The procedure is repeated for the negative emission in the cleaned datacube. The fidelity criterion (e.g., Walter et al. 2016)

$$\mathrm{fidelity}(\mathrm{S/N},\ \sigma_{\mathrm{kernel}}) = 1 - \frac{N_{\mathrm{neg}}(\mathrm{S/N},\ \sigma_{\mathrm{kernel}})}{N_{\mathrm{pos}}(\mathrm{S/N},\ \sigma_{\mathrm{kernel}})} \qquad (1)$$

[9] DETECT_MINAREA = 3, DETECT_THRES = 3, DEBLEND_NTHRES = 64, DEBLEND_MINCONT = 0.005, BACK_SIZE = 64, BACK_FILTERSIZE = 4, GAIN = 6530, MAG_ZEROPOINT = 26.46, where the effective gain is computed from the exposure time and the instrument gain, and the F140W zero-point AB magnitude (26.46) is taken from the WFC3 Handbook http://www.stsci.edu/hst/wfc3/analysis/irphotzpt.

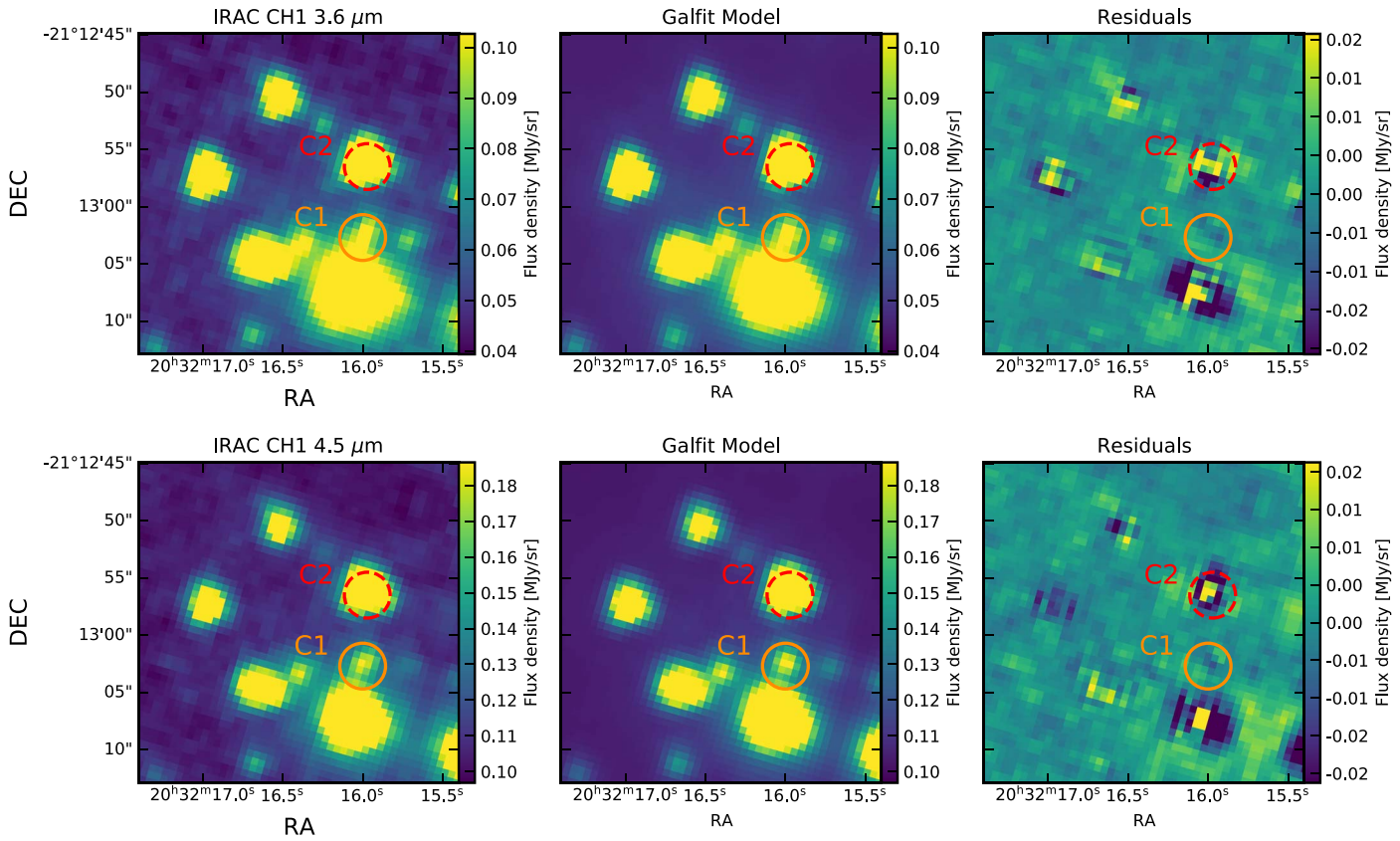

Figure 6. IRAC imaging, *GALFIT* model, and residuals for the sources PJ308-SMG1-C1/C2 (indicated with dashed red and solid orange circles, respectively). The model photometry for PJ308-SMG1-C2 (dashed red circle, not blended) is consistent with that derived by *Sextractor*. Note the significant difference in flux density range between the image and the final residual map.

Table 3
Ancillary Infrared Imaging and IFU Spectroscopic Data Available for the Three Quasars Fields

Quasar	Program ID/PI	Telescope/Instrument	Filters/$\Delta\lambda$	Exp. Time
J0305–3150	11030/R. Decarli	Spitzer/IRAC	3.6 μm, 4.5 μm	1000 s
	094.B–0893(A)/B. Venemans	VLT/MUSE	0.465–0.93 mu	2h30m
PJ231–20	14876/E. Bañados	HST/WFC3	F140W	2612 s
	099.A–0682(A)/E. Farina	VLT/MUSE	0.465–0.93 mu	3h20m
	13066/C. Mazzucchelli	Spitzer/IRAC	3.6 μm, 4.5 μm	7200 s
PJ308–21	14876/E. Bañados	HST/WFC3	F140W	2612 s
	13066/C. Mazzucchelli	Spitzer/IRAC	3.6 μm, 4.5 μm	7200 s
	099.A–0682(A)/E. Farina	VLT/MUSE	0.465–0.93 mu	5h

is used to determine the fraction of credible (e.g., not due to noise) detections as a function of S/N. Note that by definition the fidelity score is an empirical estimate of the so-called "true-positive" fraction in the final sample. In this work, we use the latest version of *FindClumps* implemented in *interferopy* (Boogaard et al. 2021).

LineSeeker (González-López et al. 2017) takes a slightly different approach than *FindClumps*, which we summarize here briefly. It starts by creating velocity-integrated maps using a Gaussian kernel rather than a boxcar. Sources are then searched using the DBSCAN algorithm on S/N > 5 pixels (Ester et al. 1996). Finally, *LineSeeker* performs a contamination analysis by injecting and retrieving mock sources in the created maps/cubes. The threshold to select significant emitters is then adjusted for each datacube by choosing the maximum acceptable false-positive rate.

Both methods were compared on the ASPECS-HUDF 3 mm data in González-López et al. (2019), who find that both methods agree relatively well, although *FindClumps* tends to slightly overestimate (by ∼7%) the S/N of faint sources (S/N ∼ 4) compared to *LineSeeker*, which could be explained by the different convolution kernels.

We run *LineSeeker* and *Findclumps* on the continuum-subtracted cleaned data cubes of the targeted 17 SMGs to generate a first list of candidate line emitters. We select a fidelity/true-positive threshold of 90% for *Findclumps* and, accordingly, a false-positive probability threshold of 10% for *LineSeeker* (both criteria are roughly equivalent to a nominal S/N ∼ 5 cut). The candidates close (<2″) to the edge of the map or near any continuum sources (<4″ from the center of any continuum source) are both discarded to remove artifacts due to the edge of the map or poor continuum subtraction,

Table 4
Ancillary Photometry for the Continuum-detected ALMA Sources

ID	F140W	[3.6 μm]	[4.5 μm]	$S_{850\ \mu m}$ (mJy)	$S_{450\ \mu m}$ (mJy)
PJ231-SMG1-C1	…[a]	22.08 ± 0.08	21.58 ± 0.13	<7.36	<46.8
PJ231-SMG1-C2	…	22.25 ± 0.09	21.18 ± 0.09	<7.36	<46.8
PJ231-SMG2-C1	25.080 ± 0.075[b]	22.79 ± 0.12	21.55 ± 0.11	<6.66	<46.8
PJ231-SMG3-C1	…	20.05 ± 0.02	19.34 ± 0.02	<6.96	<46.8
PJ231-SMG5-C1	…	…	…	<4.8	<127.69
J0305-SMG2-C1	…	22.08 ± 0.10	20.66 ± 0.10	<7.8	<46.8
J0305-SMG4-C1	…	20.80 ± 0.05	19.97 ± 0.06	<7.38	<46.8
PJ308-SMG1-C1	…	21.58 ± 0.55	20.77 ± 0.44	<11.29	<46.8
PJ308-SMG1-C2	…	19.23 ± 0.01	18.52 ± 0.01	<11.29	<46.8
PJ308-SMG2-C1	…	20.42 ± 0.03	19.70 ± 0.02	<7.35	<78.64
PJ308-SMG2-C2	…	21.33 ± 0.06	21.00 ± 0.06	<7.35	<78.64
PJ308-SMG3-C1	…	20.58 ± 0.03	19.85 ± 0.02	<6.22	<46.8
PJ308-SMG4-C1	24.170 ± 0.050	22.06 ± 0.08	21.22 ± 0.06	<4.41	<46.8
PJ308-SMG6-C1	…	21.98 ± 0.07	21.01 ± 0.05	<5.02	<82.40
PJ308-SMG9-C1	$<23.559 \pm 0.022$[c]	20.56 ± 0.02	19.81 ± 0.02	<5.35	<46.8

Notes. The HST and IRAC photometry are given in AB magnitudes. We use the detections in SCUBA2 850–450 μm maps as upper limits since the sources are unresolved (see discussion on the multiplicity in Section 3.2).
[a] Sources without HST or Spitzer photometry are not covered by the imaging available, and thus no upper limits are available.
[b] Resolves to multiple sources in the HST images (see Appendix C).
[c] The source is on the edge of the F140W imaging, with $\gtrsim$50% of the flux lost, and the F140W magnitude is therefore not considered for the SED fitting.

respectively. This results in 10 *LineSeeker* detections and 11 *Findclumps* detections, which contain the 10 candidates found by LineSeeker (e.g., *FindClumps* only finds one additional candidate at the S/N threshold chosen[10]). As for continuum sources (see Section 3), a spectrum is then extracted with an $r = 2''$ aperture at the position of each candidate, and we fit the emission line with a Gaussian profile to create a velocity-integrated line map (see Appendix D). The secure line emitters, tentatively identified as $[C\,II]_{158\ \mu m}$ emitters at $z > 6$, and their properties are listed in Table 5.

The line emitters found with *LineSeeker* and *FindClumps* are not necessary $[C\,II]_{158\ \mu m}$ at the quasar redshift. Indeed, a large fraction of them are found in the second spectral tuning of ALMA, e.g., ∼16 GHz from the high-redshift quasar $[C\,II]_{158\ \mu m}$ emission. Even candidate $[C\,II]_{158\ \mu m}$ lines in the correct spectral tuning could be low-redshift CO interlopers or simply spurious noise. Indeed, the fact that all detections have an S/N only slightly above the threshold chosen to select line emitters suggests that a large fraction are not real sources. We do not perform a photometric redshift analysis similar to that done for the continuum sources in Section 3.4, as all of our line emitters (except one, PJ231-SMG2-spwAmm.03, $m_{F140W} = 25.89 \pm 0.08$) are undetected in the SCUBA2, Spitzer/[3.6]–[4.5], and HST/F140W imaging.

Nonetheless, if some or all of these emitters are indeed $[C\,II]_{158\ \mu m}$ close to the quasar redshift, they should cluster in velocity space around the quasar redshift. We present the distribution in velocity space of the line emitters, assuming the line $[C\,II]_{158\ \mu m}$, in Figure 8. We find no evidence for an increased number of line emitters in the vicinity of the quasar redshifts, suggesting that most or all of these detections are not associated with the quasars. This is in agreement with the findings of Decarli et al. (2020), who find that in a blank field observed with ALMA Band 6 $[C\,II]_{158\ \mu m}$ emission at $z > 6$ accounts for $< 1\%$ of the flux seen in the lines, which are overwhelmingly lower-redshift CO emitters.

[10] This line emitter (J0305-SMG2-spwA-4636) is nominally detected by *LineSeeker* at S/N = 5.3, and the false-positive probability based on simulated cubes is 5%. However, the *LineSeeker* Poisson statistic false probability is 31%, which removed this emitter from the final *LineSeeker* selection.

5. MUSE Archival Data and LAEs

The three quasars studied with ALMA and SCUBA2 in this paper all have archival MUSE observations (see Table 4) published and discussed in various papers (e.g., Farina et al. 2017; Drake et al. 2019; Farina et al. 2019; Venemans et al. 2019). As discussed in the introduction, the presence of an LAE in the field of J0305–3150 was reported by Farina et al. (2017). However, systematic searches for MUSE LAEs at the redshift of PJ231–20 and PJ308–21 have not been reported. Meyer et al. (2020a) searched several quasars fields, including those of PJ231–20 and PJ308–21, to find LAEs in the redshift range probed by the Lyα forest of the quasars, and only published those detections. The search for LAEs also covered the redshift range around the quasars, and we now report the result of this search.

The MUSE archival observations of the three quasar fields were reduced and searched for LAEs in Meyer et al. (2020a), to which we refer for further details. Briefly, the data cubes were reduced using the standard ESO pipeline recipes, and sky emission contamination was removed using the Zurich Atmospheric Purge (ZAP) code (Soto et al. 2016). The reduced data cubes were then searched for Lyα emitters using two different software packages: *MUSELET* (Bacon et al. 2016) and *LSDCat* (Herenz & Wisotzki 2017). On the one hand, *MUSELET* creates narrow-band (NB) slices from the IFU data and then uses *Sextractor* to identify significant sources in the subimages and finally groups detections at close separation in wavelength-adjacent images. On the other hand, *LSDCat* runs a 3D Gaussian-matched filter on the median-filtered cube. Meyer et al. (2020a) concluded that the use of the two algorithms is beneficial since they are complementary and do not perform similarly for faint emitters or emitters close to bright continuum sources.

We searched for LAEs in the MUSE data in the fields of PJ231–20, PJ308–21, and J0305–3150 using *LSDCat* and *MUSELET* with parameters described in Meyer et al. (2020a).

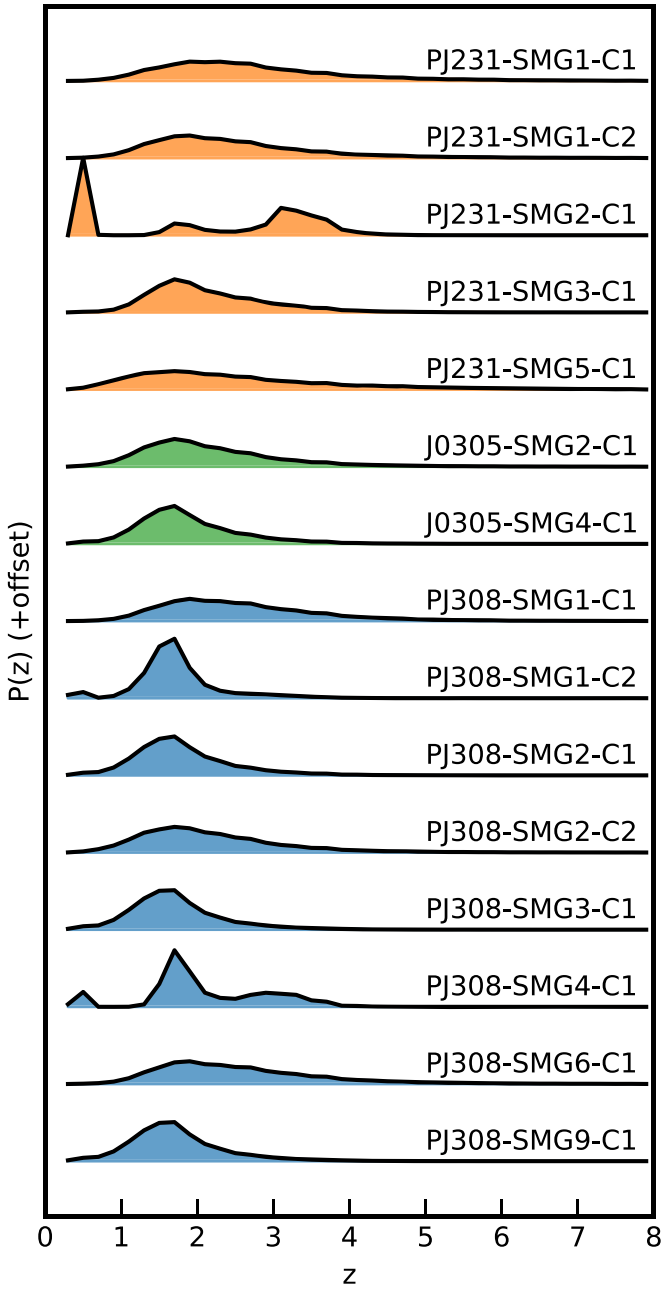

Figure 7. Posterior distributions for the photometric redshifts of the ALMA-detected SMGs obtained from *MAGPHYS-photoz* (Battisti et al. 2019) using HST F140W, IRAC, ALMA Band 6, and SCUBA2 imaging. None of the sources have a photo-z consistent with those of the background quasars ($z > 6$).

Briefly, we use the standard 6.25 Å width for the NBs created by *MUSELET* with *DETECT_MINAREA* = 4, *DETECT_THRESH* = 2.0, and *ANALYSIS_THRESH* = 2.0 *Sextractor* parameters for the NB search. We use the standard continuum width (4 times wider than the NBs) for continuum subtraction. For *LSDCat* we use a Gaussian convolution kernel with the default polynomial coefficients for the PSF FWHM dependence on wavelength, make use of the optional median filtering, and impose an S/N threshold >8 to select pixels with significant flux. All candidates were subsequently visually inspected. Typical contaminants are artifacts due to poor continuum subtraction, nearby extended sources with strong emission lines, low-redshift [OII] doublets, and cosmic rays (see further Appendix B of Meyer et al. 2020a). Low-redshift [OII] $\lambda\lambda$3727, 3729 doublets (with a peak separation of $\sim$220 km s^{-1}) are easily resolved in the MUSE data with a resolution of 75 km s^{-1} at 9300 Å, where $z = 6.6$ Lyα is searched for. While double-peaked emission could potentially be a high-redshift double-peaked Lyα profile (e.g., Hu et al. 2016; Matthee et al. 2018; Songaila et al. 2018; Meyer et al. 2020b; Bosman et al. 2020), such profiles are expected to be exceedingly rare at $z > 5.5$ (e.g., Garel et al. 2021; Gronke et al. 2021). Additionally, the [OII] doublet presents a relatively constant ratio (e.g., Paulino-Afonso et al. 2018), making it easy to discard such contaminants. Other low-redshift interlopers (e.g. Hβ+[OIII], Hα) are identified and removed owing to the presence of other multiple lines in the MUSE wavelength range. We have verified that LAEs are not detected in the continuum image produced from the MUSE cube.

From this search, we selected galaxies with velocity separation $\pm$1000 km s^{-1} from the central quasar [C II]$_{158\,\mu m}$ redshift.[11] Only two such LAEs were found, both in the field of PJ231–20, with no candidates at the redshift of PJ308–21 and J0305–3150. PJ231–20 is thus the only quasar with two relatively bright LAEs (within $\pm$1000 km s^{-1}) at $z \gtrsim 5.5$. The LAEs around PJ231–20 were found at a distance of $r_\perp = 0.562$ cMpc and $r_\perp = 0.287$ cMpc from PJ231–20 and have an Lyα luminosity $L_{\mathrm{Ly}\alpha} > 3 \times 10^{42}$ erg s^{-1} (see Table 6). Both LAEs were detected with *LSDCat* but not recovered by *MUSELET* using standard parameters.[12] One of the LAEs is detected in the F140W image, and both are undetected in the IRAC data (see Figure 9). At these Lyα luminosities, the number density of LAEs in a blank MUSE field is $\sim$(1–5) $\times$ 10^{-4} cMpc^{-3} (Drake et al. 2017; Konno et al. 2018; de La Vieuville et al. 2019), which for the volume probed (50″ $\times$ 50″ $\times$ 2000 km s^{-1} $\sim$ 80 cMpc^3 at $z = 6.6$) implies 0.009–0.04 LAEs per field, making the environment of PJ231–20 extremely overdense.

The search did not, however, recover the LAE reported by Farina et al. (2017) near the redshift of the quasar J0305–3150. The reason for this is that the LAE is extremely close to the quasar (2.″3, e.g., $\sim$9 pixels offset). As the quasar and the LAE emit at the same wavelength, they are connected in the >8σ thresholded S/N cube and considered as one unique source by *LSDCat*. Similarly, *MUSELET* did not recover the emitter, as it is very faint and not extended. Farina et al. (2017) recovered the LAE by using wider pseudo-NB images (10 Å vs. 6.25 Å in MUSELET) and by using a lower threshold for the NB search (1.5σ vs. 2.0σ). In either case, the parameters of *LSDCat* and *MUSELET* can be adapted to recover this specific emitter at the cost of losing others or increasing the number of spurious sources over the full datacube. While this would suggest that combining the different LAE search methods is the way forward, this would result in a complex selection function that might be a hindrance to future statistical analyses. We therefore do not attempt to perform a search similar to that of Farina et al. (2017) in the fields of PJ308–21 and PJ231–20.

[11] Note that the Lyα redshift of the emitters is corrected toward the systemic redshift using the apparent FWHM method of Verhamme et al. (2018).

[12] *MUSELET* runs *Sextractor* on 6.25 Å wide NB images, which would only contain a fraction of the flux of a high-redshift Lyα line, therefore detecting only the strongest lines. We have verified that reducing the detection significance and mininum area thresholds in the *Sextractor* parameters leads to the recovery of the two LAEs with *MUSELET*.

Table 5
Line Emitters Recovered with *LineSeeker* and *Findclumps* in the ALMA Pointings Studied in This Work

Name	R.A.	Decl.	Freq (GHz)	S/N	$r_\perp$ (cMpc)	Δv (km s^{-1})
PJ231-SMG1-spwAmm.01	15:26:40.30	−20:51:03.70	250.924	5.5	2.95	490
PJ231-SMG2-spwAmm.01	15:26:39.33	−20:50:38.90	249.909	5.2	1.79	−730
PJ231-SMG2-spwAmm.03[a]	15:26:37.89	−20:50:54.90	248.698	4.9	2.23	−2180
J0305-SMG2-spwAmm.01	03:05:23.38	−31:49:44.40	250.565	5.7	4.49	1160
J0305-SMG2-spwAmm.02	03:05:21.78	−31:49:50.40	249.53	5.7	3.71	−80
J0305-SMG2-spwA-4636[b]	03:05:22.30	−31:50:03.52	250.838	5.7	3.55	1490
PJ308-SMG4-spwBmm.01	20:32:07.33	−21:14:03.30	249.164	5.4	1.60	−15470
PJ308-SMG6-spwBmm.01	20:32:09.62	−21:16:00.90	246.781	5.6	4.80	−18200
PJ308-SMG6-spwBmm.02	20:32:08.69	−21:16:12.70	249.418	5.4	5.34	−15180
PJ308-SMG6-spwBmm.03	20:32:08.41	−21:16:14.50	247.504	5.3	5.43	−17370
PJ308-SMG9-spwBmm.02	20:32:13.08	−21:14:31.70	246.937	5.4	2.03	−18020

Notes. The last two columns give the proper transverse distance (assuming that the line is [C II]$_{158\ \mu m}$ close to the redshift of the quasar) and velocity offset from the quasar [C II]$_{158\ \mu m}$ redshift.
[a] Detected in the HST imaging with $m_{F140W} = 25.89 \pm 0.08$.
[b] Only selected with *FindClumps*.

Table 6
Properties of New Lyα Emitters Discovered in the Field of PJ231–20

R.A.	Decl.	$z_{Ly\alpha}$	FWHM (km s^{-1})	z_{corr}^{a}	$L_{Ly\alpha}$[b] (10^{42} erg s^{-1})	m_{F140W}	EW$_{rest}$(Lyα) (Å)	$r_\perp$ (cMpc)
15:26:36.91	−20:49:53.47	6.592	121.9	6.590	3.3 ± 0.5	25.9 ± 0.1	23.5 ± 3.3	0.562
15:26:37.90	−20:50:05.87	6.598	162.4	6.596	5.4 ± 0.5	<27.1	>118	0.287

Notes. Limits are given at the 3σ level. The EW width is computed using the continuum UV flux at 1500 Å (rest-frame) derived from the m_{F140W} magnitude assuming a flat f_ν spectrum.
[a] The corrected redshift is derived using the observed FWHM following the empirical correction calibrated on low-redshift LAEs by Verhamme et al. (2018).
[b] The luminosities are derived using the flux extracted in a (+300, −300) km s^{-1} window centered on the peak of the emission.

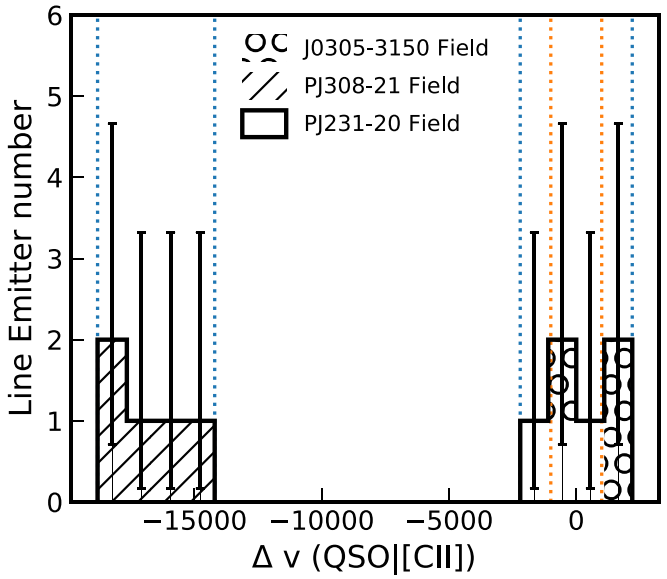

Figure 8. Velocity offset distribution of line (continuum-free) emitters detected in the SMG fields, assuming that the line is [C II]$_{158\ \mu m}$. The vertical blue bars show the velocity range of the two spectral windows of the ALMA tunings, and the vertical orange bars show the interval (−1000, 1000) km s^{-1} around the quasar redshift where an overdensity would be expected. The error bars are Poisson uncertainties on the number of detected sources (Gehrels 1986). The absence of clustering around the quasar in velocity space could suggest that most emitters are foreground CO sources.

6. The Varied Environments of High-redshift Quasars

We now characterize the cross-correlation of $z > 6$ quasars and galaxies with our updated constraints. A common approximation of the galaxy–quasar cross-correlation is a simple power-law relation (see, e.g., Hennawi et al. 2006; Kayo & Oguri 2012; Eftekharzadeh et al. 2017; Farina et al. 2017; García-Vergara et al. 2017; Eftekharzadeh et al. 2019; Farina et al. 2019; García-Vergara et al. 2019)

$$\xi^{QG}(r) = \left(\frac{r}{R_0^{QG}}\right)^{-\gamma}, \quad (2)$$

where r is the 3D comoving distance between the quasar and the galaxy, $\gamma = 1.8$–2.0 is the slope of the clustering strength, and $R_0^{QG} = \sqrt{R_0^{GG} R_0^{QQ}}$ is the quasar–galaxy cross-correlation length, which can be inferred from the quasar and galaxy autocorrelation length. For the purpose of this discussion, we use the LAE autocorrelation length measured by Ouchi et al. (2010; $r_0^{GG} = 10.3^{+4.7}_{-8.6}$ cMpc) and assume the Shen et al. (2007) quasar correlation length ($r_0^{QQ} = 17.4^{+2.5}_{-2.8}$ cMpc) derived from $z > 2.9$ Sloan Digital Sky Survey quasars.

We summarize the updated constraints on the overdensity of galaxies in the fields of high-redshift quasars in Figure 10. On the one hand, our constraints at large scale (∼1.8–5.8 cMpc) on 17 pointings show that the overdensity of [C II]$_{158\ \mu m}$ emitters declines with distance, in agreement with the simple model described above. In fact, the detection of a single SMG in [C II]$_{158\ \mu m}$ at the redshift of the quasar would have implied a number density of [C II]$_{158\ \mu m}$ emitters close to that found on smaller scales, and thus an extremely high correlation strength or length. On the other hand, our LAE search results support earlier findings that LAEs are overdense in quasar fields (Farina et al. 2017; Mignoli et al. 2020). However, their overdensity is an order of magnitude below that of

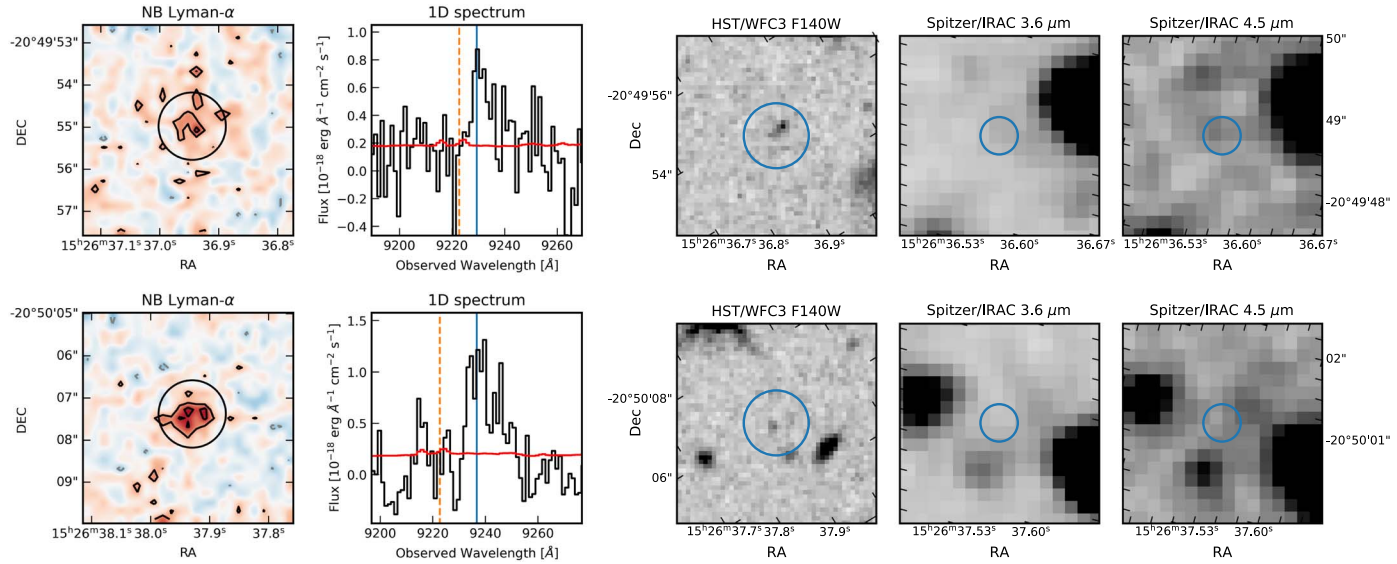

Figure 9. LAEs found at the redshift of PJ231–20 in the archival MUSE data. The leftmost panel shows the pseudo-narrowband image centered on the peak of the emission. The contours (negative in dashed gray, positive in black) mark the (−4, −2, 2, 4) surface brightness rms levels. The second-leftmost panel shows the extracted Lyα spectrum (black) and error array (red), extracted in an $r = 0\farcs8$ aperture shown in the leftmost panel. The blue vertical line indicates the redshift of the Lyα emitter determined by *LSDCat* from the Gaussian-filtered cube. The wavelength of the redshifted Lyα line of the quasar is indicated by a vertical orange dashed line. The last panels show the F140W and IRAC imaging, with the position of the LAE marked with an $r = 1''$ aperture circle (blue).

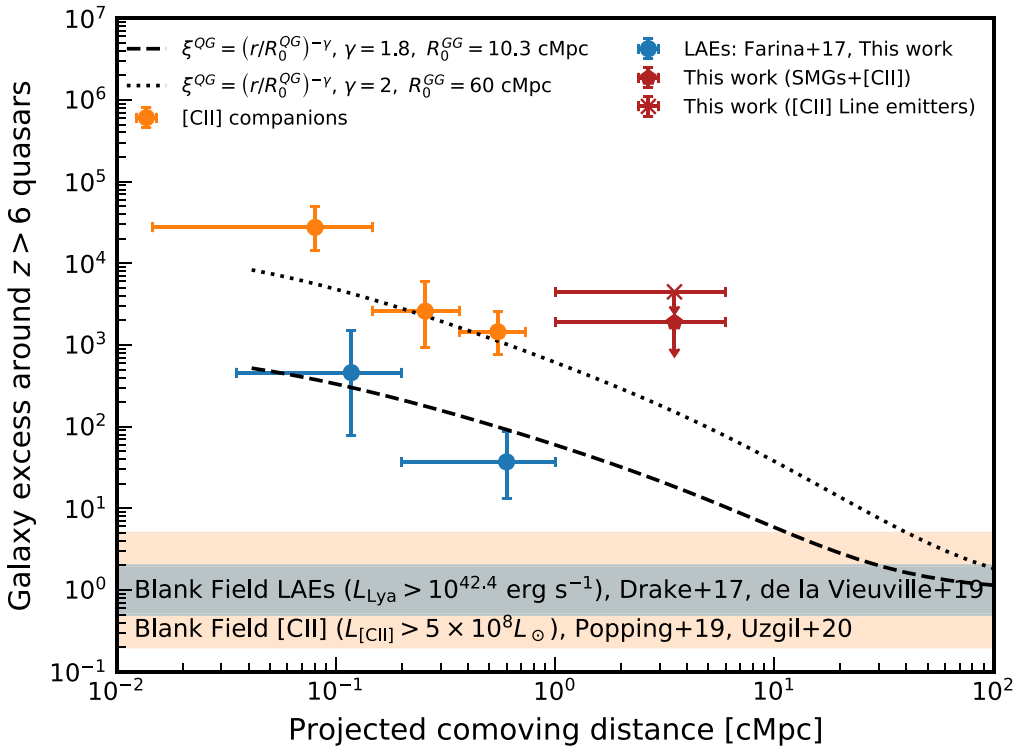

Figure 10. Excess number density of galaxies around $z > 6$ quasars searched for [C II]$_{158\ \mu m}$ or LAE companions. The observed number densities of [C II]$_{158\ \mu m}$ emitters and LAEs are divided by the blank-field number densities of Popping et al. (2019); Uzgil et al. (2021) and Drake et al. (2017); de La Vieuville et al. (2019), respectively, integrated down to the limits of $L_{[CII]} = 5 \times 10^8\ L_\odot$ and $L_{Lya} = 10^{42.4}$ erg s^{-1}, respectively. The upper limits from this work are derived using the 2σ single-sided upper-limit Poisson errors (Gehrels 1986) on the number of continuum+[C II]$_{158\ \mu m}$ sources (0, e.g., $< 3.783(2\sigma)$) and [C II]$_{158\ \mu m}$-only emitters (3, e.g., $< 8.9(2\sigma)$) divided by the volume surveyed and the blank-field [C II]$_{158\ \mu m}$ number density. The dashed and dotted lines give the expectation for an approximated quasar–galaxy cross-correlation (see text for details).

[C II]$_{158\ \mu m}$ companions found in single ALMA pointings centered on the quasars. The fiducial model of the quasar-LAE cross-correlation ($\gamma = 1.8$, $R_0^{GG} = 10.3$ cMpc) matches very well the observed number densities, whereas the quasar–[C II]$_{158\ \mu m}$ emitters clustering is only well reproduced with a much larger clustering length ($R_0^{GG} = 60$ cMpc) and $\gamma = 2$.

This difference in clustering strength (one order of magnitude at $\sim$1 cMpc) could signal either a strong bias toward dusty sources around quasars or a large host halo mass for [C II]$_{158\ \mu m}$ emitters. Unfortunately, the $z \sim 6$ [C II]$_{158\ \mu m}$ autocorrelation and host halo mass are not well constrained, and we cannot definitely conclude. However, García-Vergara

et al. (2017, 2019, 2021) find similar results at $z \sim 4$, where CO emitters and LBGs are more strongly clustered around quasars than LAEs. They suggest that a bias toward dusty galaxies in the environment of massive quasars could suppress the number of galaxies detected with the Lyα line that are strongly absorbed by dust. However, in their measurement the number of LAEs around quasars is inferior to that inferred from the cross-correlation model detailed above, whereas in our case the fiducial model matches the data well (although the uncertainties and cosmic variance are still large). One possibility is that the quasar radiation carves out an ionized region boosting the Lyα transmission in nearby galaxies (e.g., Bosman et al. 2021), offsetting some of the bias toward more dusty galaxies, which should decrease the number of LAE detections.

In the context of this hypothesis, it is interesting to note that the closest LAE to the PJ231–20 was not detected in previous ALMA [C II]$_{158\,\mu m}$ observations of the quasar (Decarli et al. 2017; Venemans et al. 2020), despite being within the ALMA field of view. This sets a lower limit for the [C II]$_{158\,\mu m}$ flux density of this source at $S_\nu \Delta v \lesssim 0.1$ Jy km s^{-1} at the 5σ level (assuming an FWHM of 300 km s^{-1}), which can be translated to a line luminosity $L_{[CII]} \lesssim 10^8\ L_\odot$ and star formation rate $\mathrm{SFR_{IR}} \lesssim 10 - 30\,M_\odot\,\mathrm{yr}^{-1}$ using standard scaling relations (e.g., Herrera-Camus et al. 2018). Conversely, the [C II]$_{158\,\mu m}$ companions reported in Decarli et al. (2017), Neeleman et al. (2019), and Venemans et al. (2020) around the three quasars are not seen in Lyα in the MUSE data and therefore have $L_{\mathrm{Ly}\alpha} \lesssim 2 \times 10^{42}$ erg s^{-1}. Following, e.g., Sobral et al. (2018), assuming case B recombination, a 10% escape fraction of Lyman continuum photons (Meyer et al. 2020a), and a 20% escape fraction of Lyα photons, we can put an approximate upper limit on the $\mathrm{SFR_{Ly\alpha}} \lesssim 10\,M_\odot\,\mathrm{yr}^{-1}$. On the one hand, the [C II]–SFR relationship used above assumes that most of the UV emission is absorbed by dust and reemitted in the infrared, and thus becomes inefficient for dust- and metal-poor galaxies. On the other hand, the Lyα−SFR relation assumes an average escape fraction of Lyα photons and would thus underestimate the SFR if the LAEs were dust-rich (thus absorbing more Lyα photons than expected). The fact that [C II]$_{158\,\mu m}$-detected sources are not detected in Lyα, at the same nominal SFR limits, suggests that we are looking at a dichotomy of metal-poor and metal-rich, dusty galaxies detected at different wavelengths. This dichotomy might be only apparent as we sample the extremes of the obscured-to-unobscured SFR distribution, and deeper observations might change this picture. What is interesting, however, is that high-redshift quasars cluster more strongly with [C II]$_{158\,\mu m}$ emitters (dust-rich) than LAEs, in agreement with results at $z \sim 4$ (García-Vergara et al. 2021). This suggests that more evolved and dusty galaxies are found around quasars, which would be expected if they trace the first large-scale structure in the universe. Finally, the clustering strength discrepancy between the LAEs and [C II]$_{158\,\mu m}$ emitters might be even larger, as the number of LAEs could preferentially be increased by the presence of the quasar ionization zone facilitating the escape of Lyα photons (e.g., Bosman et al. 2021).

7. Conclusion

We searched the fields of three high-redshift quasars (J0305–3150, PJ2310–20, PJ308–21) for galaxy overdensities using three approaches: (1) confirming the redshift of 17 bright SCUBA2-selected SMGs with ALMA, (2) a blind search for [C II]$_{158\,\mu m}$ emitters in these 17 ALMA pointings, and (3) a search for LAEs using archival MUSE observations. We report the following findings:

1. With ALMA (Band 6) we detect the continuum of 12 out of 17 SCUBA2 SMGs targeted, and we find that 3 have two detected counterparts in the ALMA continuum maps. The confirmation rate with ALMA and the multiplicity fraction are in good agreement with that of earlier SMG follow-up studies with ALMA (e.g., Hodge et al. 2013).
2. We find no [C II]$_{158\,\mu m}$ lines in the SMGs at a similar redshift of the $z > 6$ quasars in the field. The absence of [C II]$_{158\,\mu m}$ is unlikely if these sources are indeed at the quasar redshift, considering their continuum flux densities and the usual [C II]$_{158\,\mu m}$/FIR luminosity ratio in low- and high-redshift galaxies. Moreover, the photometric redshifts derived using HST, Spitzer, SCUBA2 and ALMA Band 6 imaging disfavor any high-redshift ($z > 3$) solutions. We thus conclude that all the SMGs are foreground sources.
3. We report the detection of emission lines in four SMGs in the field of PJ231–20 consistent with CO 7–6 and [C I]$_{809\,\mu m}$ at $z \simeq 2.4$. This overdensity of sources is located at the redshift of an Mg II absorber in the quasar spectrum. This supports the previous finding that none of the SMGs are high-redshift ($z > 6$) sources.
4. Our blind search for [C II]$_{158\,\mu m}$ emitters at the redshift of the quasar in the SMG ALMA pointings finds no excess of sources around the quasar redshift. We conclude that most detections are low-redshift CO interlopers.
5. We report the discovery of two previously unpublished LAEs at the redshift of PJ231–20, indicating an overdensity in this field. We found, however, no LAEs around PJ308–21 and J0305–3150. We did not recover the LAEs found by Farina et al. (2017), which can be explained by the different search methods. Overall, we find an overdensity of LAEs in our quasars fields, supporting earlier results on quasar–LAE overdensities (Farina et al. 2017; Mignoli et al. 2020).

Although our [C II]$_{158\,\mu m}$ nondetections could be due to cosmic variance, our results suggest that targeting bright SMGs is not the most promising way forward to characterize the overdensities of galaxies around high-redshift quasars. Additionally, the combination of MUSE and ALMA data on the same field suggests a dichotomy of dust-rich/dust-poor sources that cannot yet be satisfyingly explained. Blind searches taking advantage of wide-field and frequency coverage, such as provided by large mosaics with ALMA, MUSE, and JWST, might thus be the only way to map and understand the large-scale environment of quasars in the first billion years.

The authors thank the referee for useful suggestions that improved the manuscript. R.A.M. and F.W. acknowledge support from the ERC Advanced grant 740246 (Cosmic_Gas).

This paper makes use of the following ALMA data: ADS/JAO.ALMA#2019.1.01003.S. ALMA is a partnership of ESO (representing its member states), NSF (USA) and NINS (Japan), together with NRC (Canada), MOST and ASIAA (Taiwan), and KASI (Republic of Korea), in cooperation with the Republic of Chile. The Joint ALMA Observatory is operated by ESO, AUI/NRAO and NAOJ. Based on observations made with ESO

Telescopes at the La Silla Paranal Observatory under program ID 094.B-0893(A), 099.A-0682(A), 099.A-0682(A).

These HST observations are associated with program 14876. Support for this work was provided by NASA through grant No. 10747 from the Space Telescope Science Institute, which is operated by AURA, Inc., under NASA contract NAS 5-26555. This work is based (in part) on observations made with the Spitzer Space Telescope (program IDs 11030, 13066), which was operated by the Jet Propulsion Laboratory, California Institute of Technology, under a contract with NASA.

The James Clerk Maxwell Telescope is operated by the East Asian Observatory on behalf of the National Astronomical Observatory of Japan; Academia Sinica Institute of Astronomy and Astrophysics; the Korea Astronomy and Space Science Institute; the National Astronomical Research Institute of Thailand; and Center for Astronomical Mega-Science (as well as the National Key R&D Program of China with No. 2017YFA0402700). Additional funding support is provided by the Science and Technology Facilities Council of the United Kingdom and participating universities and organizations in the United Kingdom and Canada. Additional funds for the construction of SCUBA2 were provided by the Canada Foundation for Innovation.

The authors wish to recognize and acknowledge the very significant cultural role and reverence that the summit of Maunakea has always had within the indigenous Hawaiian community. We are most fortunate to have the opportunity to conduct observations from this mountain.

Facilities: ALMA, VLT (MUSE), HST (WFC3), Spitzer (IRAC), JCMT (SCUBA2).

Software: astropy (The Astropy Collaboration et al. 2018), scipy (Virtanen et al. 2020), numpy (Harris et al. 2020), matplotlib (Hunter 2007), interferopy (Boogaard et al. 2021).

Appendix A
SCUBA2 Quasar Field Images

In this appendix we reproduce for completeness a zoomed-in version of the SCUBA2 850 μm maps (Figure 11) with the position of the quasar and the targeted SMGs highlighted. A full description of the SCUBA2 observations and data reductions will be presented in Q. Li et al., (2022, in preparation).

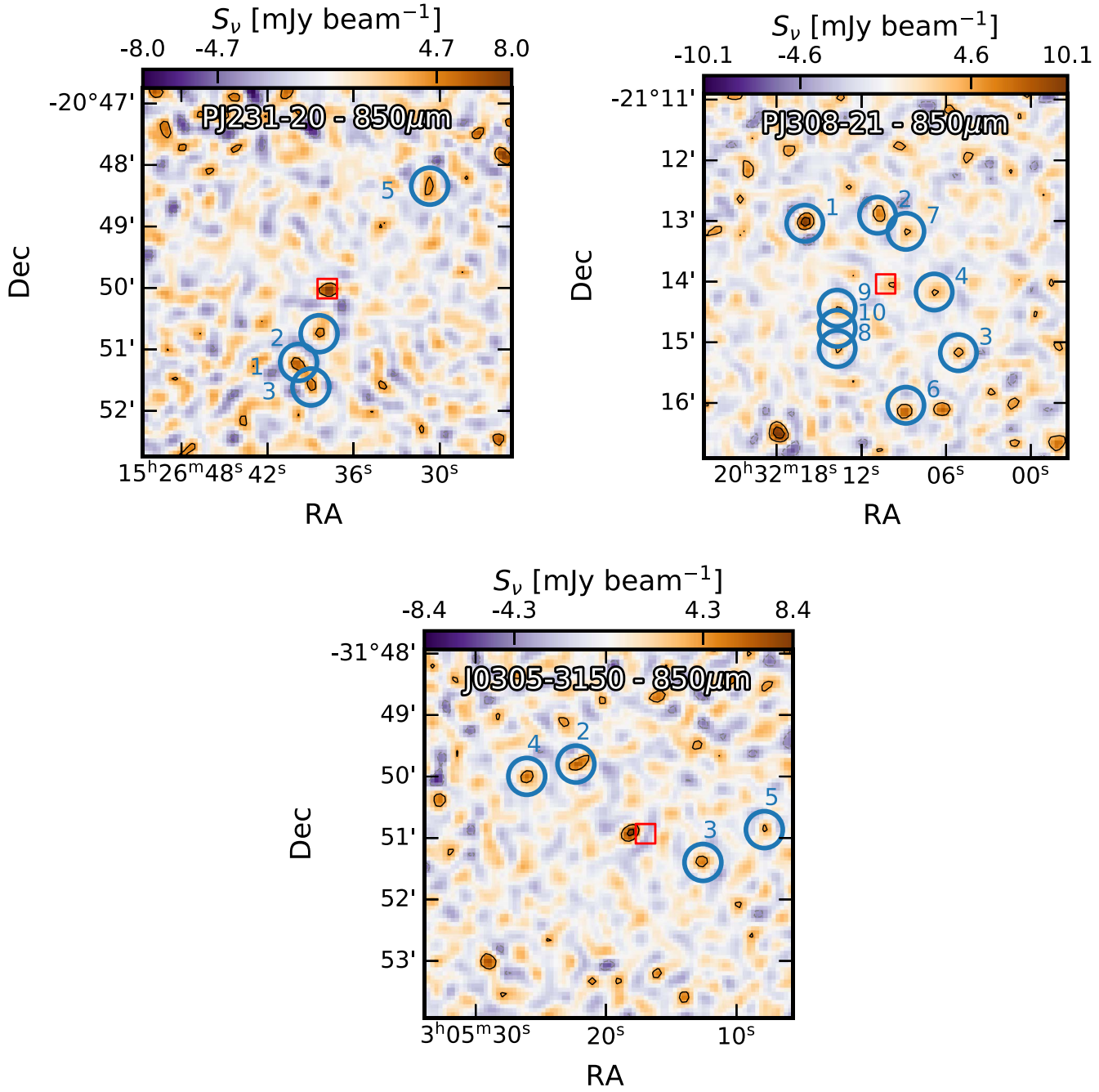

Figure 11. SCUBA2 850 μm imaging of the quasar fields of PJ231–20, PJ308–21, and J0305–3150 from Q. Li et al. (2022, in preparation), reproduced here for completeness. The $[\mathrm{C\,II}]_{158\ \mu\mathrm{m}}$ position of the quasar is highlighted in a red box, and the ALMA pointings reported in this work are denoted by blue circles and numbers.

Appendix B
A $z = 2.42$ Overdensity in the Field of PJ231–20

The case of the SMGs in the field of PJ231–20 stands out from the analysis presented in Section 3. We show the aperture-integrated spectra ($r = 2''$) of the PJ231–20 sources in Figure 12. Three of these four targets show evidence for two lines that are consistent with $[\mathrm{C\,I}]_{809\ \mu\mathrm{m}}$ and CO 7–6 (806 μm) at $z = 2.412$, 2.403, and 2.429. There exists no other pair of strong atomic fine-structure lines and CO lines with similar velocity offset, and the $z \sim 2$ interpretation is supported by the photometric redshift analysis (see Figure 7). PJ231-SMG2-C1 (Figure 12, top left) does not show two clear emission lines, but one of them is exactly at the frequency of $[\mathrm{C\,I}]_{809\ \mu\mathrm{m}}$ in PJ231-SGM3-C1 (Figure 12, bottom left), the source with the most convincing $[\mathrm{C\,I}]_{809\ \mu\mathrm{m}}$/CO 7–6 spectrum, suggesting that it could be at the same redshift but with a fainter CO luminosity. Additionally, it should be noted that PJ231-SMG2-C1 resolves in two sources in the HST images and that its photometric redshift might be uncertain (see Figure 15). We provide FIR, CO, and $[\mathrm{C\,I}]_{809\ \mu\mathrm{m}}$ luminosities in Table 7. The line luminosity ratios of CO and $[\mathrm{C\,I}]_{809\ \mu\mathrm{m}}$ are close to unity in all sources where both are detected, and it is ~0.5 for PJ231-SMG2-C1, in agreement with the values found for local (U)LIRGs (e.g., Lu et al. 2017).

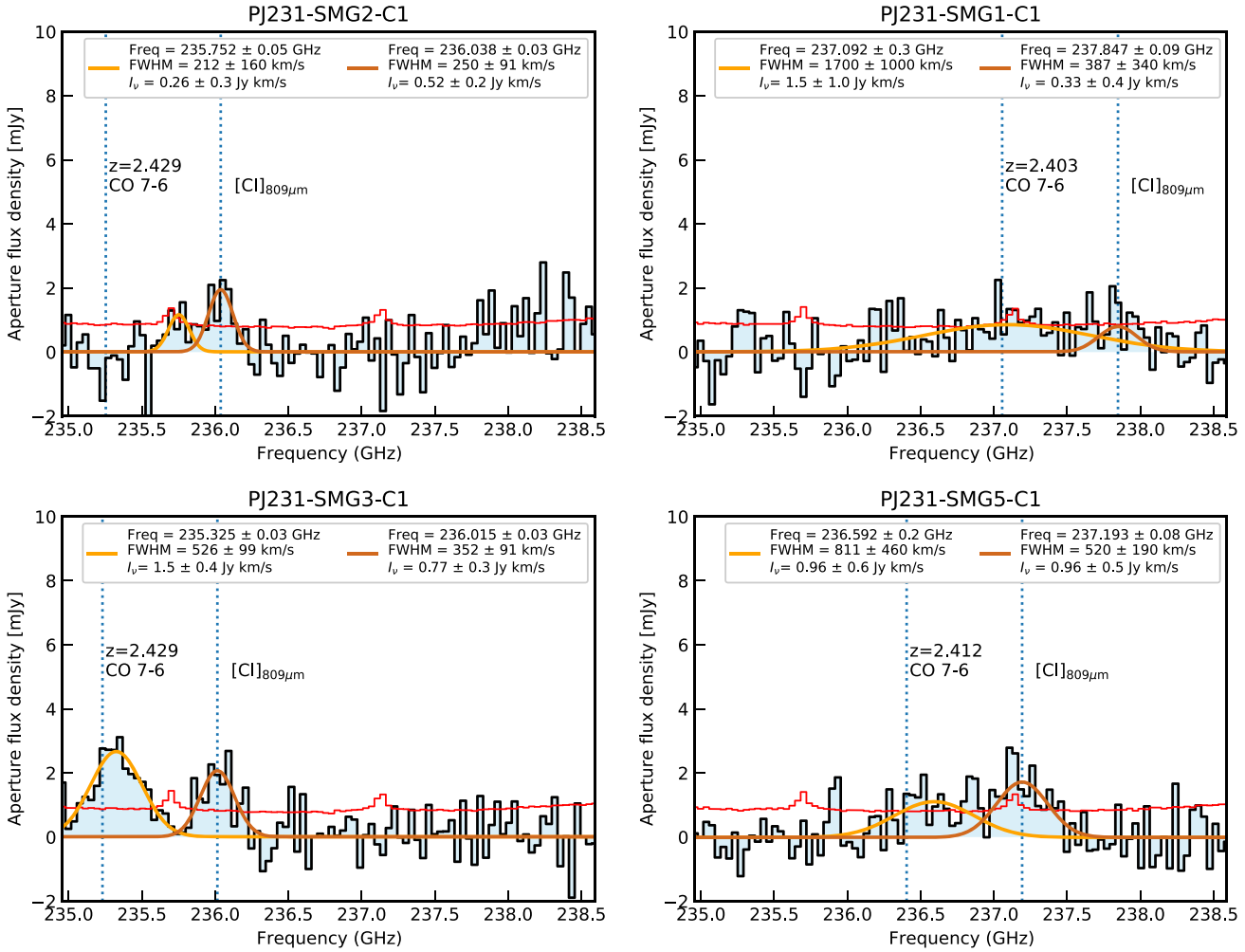

Figure 12. Aperture-integrated ($r = 2''$), continuum-subtracted spectra (black, rms error in red) of four of the five continuum sources detected in the field of PJ231–20. The error array (red) is measured for each spectrum using the rms per beam rescaled to the number beam in the $r = 2''$ aperture. Double-Gaussian profiles are fitted to the spectra (orange, dark orange) and in three objects are consistent with [C I]$_{809\ \mu m}$ and CO 7–6 (806 μm) emission at $z = 2.41$–2.42 (blue dotted vertical lines).

Table 7
Best-fit CO 7–6 and [C I]$_{809\ \mu m}$ Emission-line Properties of the $z \sim 2.4$ SMGs in the Field of PJ231–20

ID	ν_{CO} (GHz)	FWHM$_{CO}$ (km s^{-1})	L_{CO} (10^8 $L_\odot$)	$\nu_{[C\ I]}$ (GHz)	FWHM$_{[C\ I]}$ (km s^{-1})	$L_{[C\ I]}$ (10^8 $L_\odot$)	z
PJ231-SMG1-C1	237.09 ± 0.26	1700 ± 1000	1.4 ± 1.0	237.85 ± 0.08	380 ± 340	0.3 ± 0.3	2.403
PJ231-SMG2-C1	...	...	...	236.04 ± 0.03	250 ± 90	0.5 ± 0.2	2.429?
PJ231-SMG3-C1	235.33 ± 0.03	530 ± 100	1.42 ± 0.34	236.02 ± 0.03	350 ± 90	0.7 ± 0.3	2.429
PJ231-SMG5-C1	236.60 ± 0.20	810 ± 470	0.90 ± 0.58	237.19 ± 0.08	520 ± 200	0.9 ± 0.4	2.412

We hence conclude that an overdensity of $z \simeq 2.42$ SMGs lies in the field of PJ231–20. The four objects lie at projected sky distances $r_\perp \simeq 1$–4 cMpc from the quasar. Furthermore, the redshift of the four SMGs matches ($\Delta v \simeq (-820, 680, 1465)$ km s^{-1}) that of an Mg II $\lambda\lambda$2798, 2803 absorption system in the spectrum of PJ231–20 (Chen et al. 2017, system 262 in their catalog). Given that all the SMGs are at projected distances $r_\perp > 1$ comoving Mpc from the quasar sight line, none of these are expected to be the host of the absorption. Rather, they trace the overdense environment where Mg II absorbers are more likely to be found (e.g., Lee et al. 2021). We thus conclude that a $z = 2.4$ galaxy overdensity is serendipitously aligned with the high-redshift quasar PJ231–20.

Appendix C
MAGPHYS SED Best Fits

We present in this appendix the best-fit *MAGPHYS* SED resulting from our photometric redshift analysis in Section 3.4 in Figures 13 and 14. In each figure, the SED is presented in black, with the observed fluxes in orange, and the inset gives the posterior distribution of the photometric redshift. The low number of data points (up to a maximum of three detections) leads to poorly constrained photometric redshifts with an SED modeling code sampling many more parameters. As such, the best-fit SED often has a different redshift than that of the photometric redshift posterior. The photometric redshift estimates of the SMGs in the field of PJ231–20 also differ from the spectroscopic redshifts by

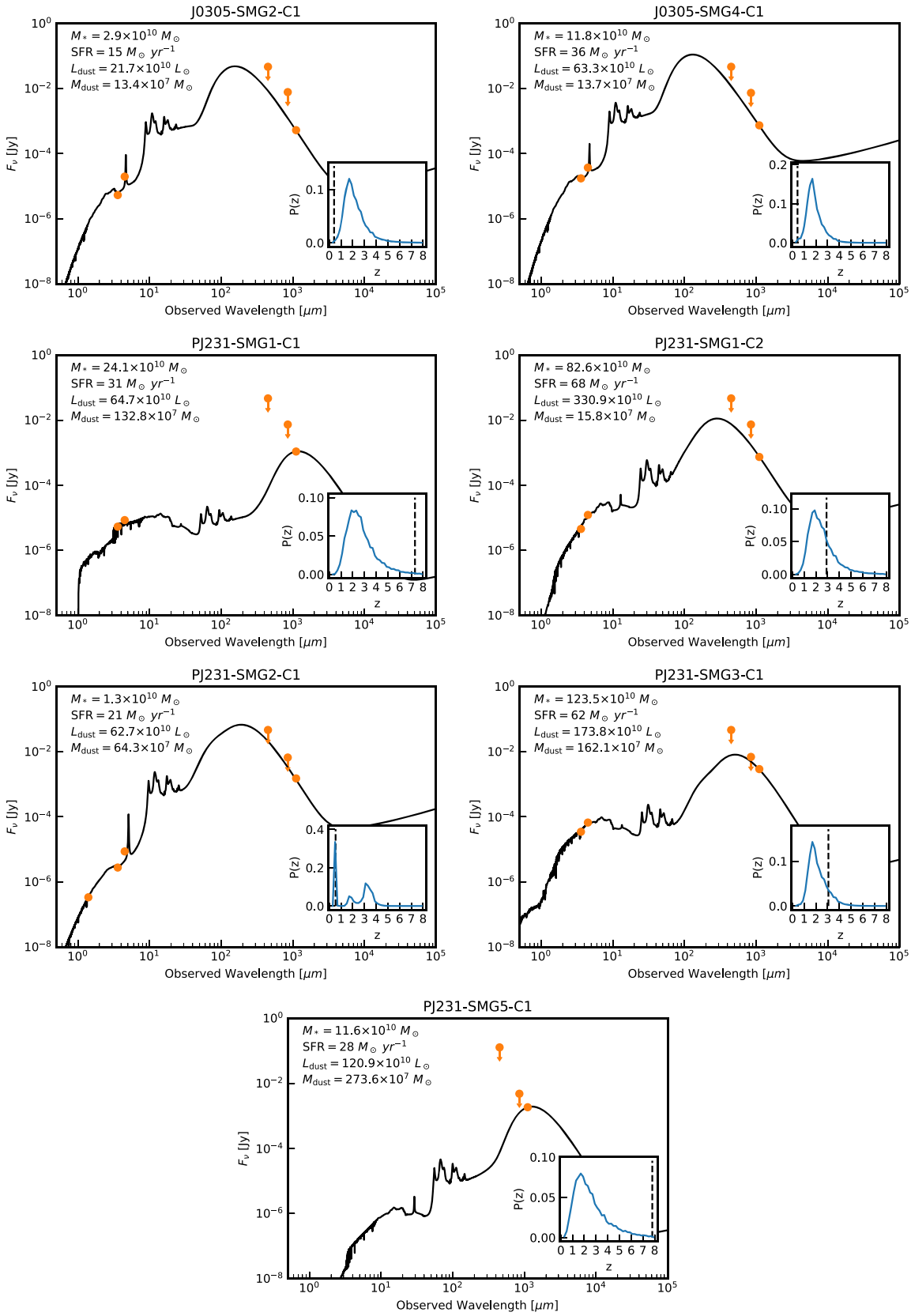

Figure 13. MAGPHYS best-fit SEDs, flux density measurements (orange), and photometric redshift posterior (inset, blue) for the continuum sources detected in our ALMA pointings (see Table 4 for the ancillary photometry). The redshift of the best-fit SED is indicated as a vertical dashed line in the inset, and its main physical parameters are indicated in the upper left corner of the main plot.

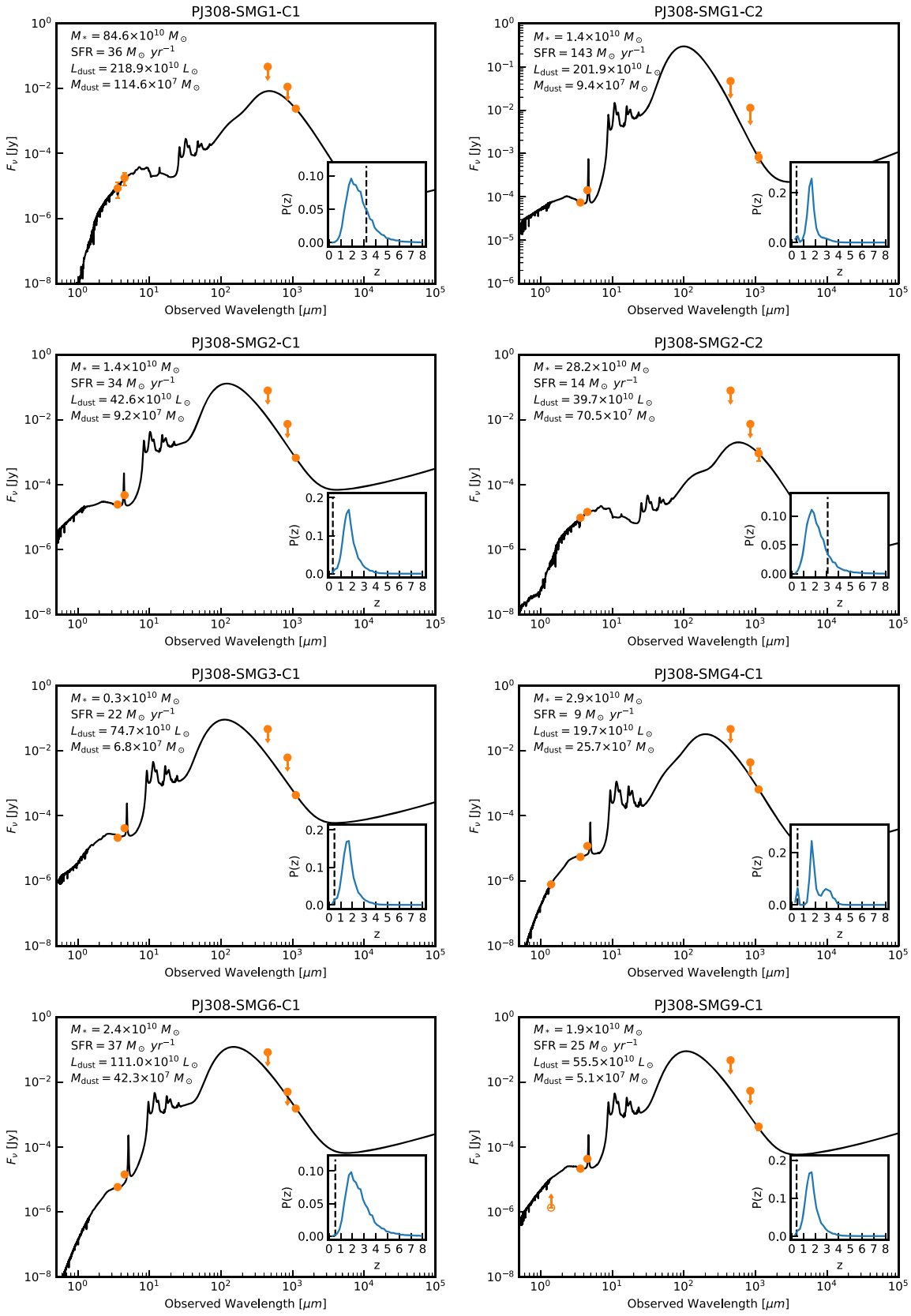

Figure 14. MAGPHYS best-fit SEDs, flux density measurements (orange), and photometric redshift posterior (inset, blue) for the continuum sources detected in our ALMA pointings (see Table 4 for the ancillary photometry). The redshift of the best-fit SED is indicated as a vertical dashed line in the inset, and its main physical parameters are indicated in the upper left corner of the main plot.

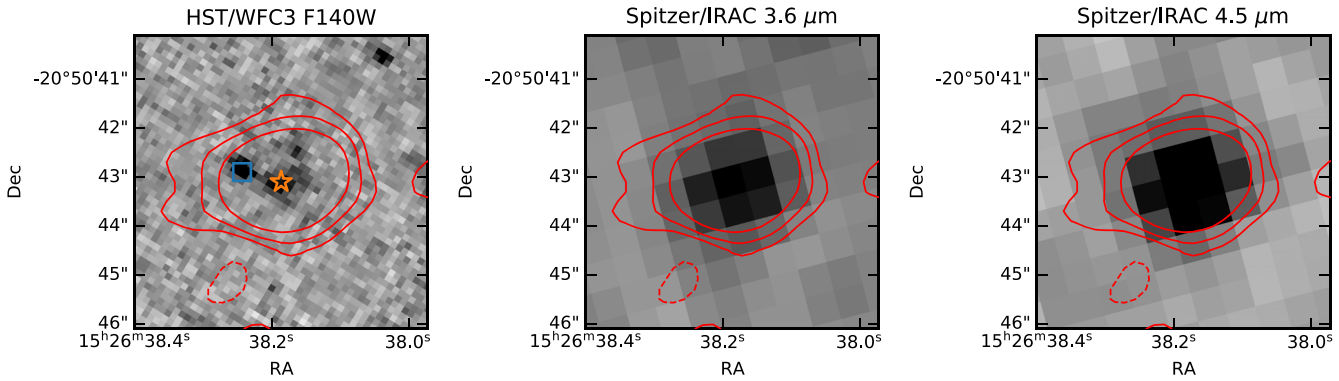

Figure 15. HST and Spitzer imaging of PJ231-SMG2-C1. The red contours show the $(-4, -2, 2, 4)\sigma$ levels of the dust continuum emission. For the purposes of the SED fitting, we assume that the central source (orange star) is the ALMA/SCUBA2 SMG. The offset source indicated by a blue square is fainter by ∼0.5 mag (F140W).

$\Delta z \sim 0.4$. Additional imaging data in the optical and submillimeter are needed to improve the SED modeling.

We also present the imaging data for PJ231-SMG2-C1 in Figure 15, which shows multiple sources in the HST imaging. For the purposes of the SED fitting, we assume that the brighter F140W central source is corresponding to the Spitzer, ALMA, and SCUBA2 detections. We do not attempt to deblend the Spitzer imaging given the lack of evidence for a second source.

Appendix D
Candidate $[\mathrm{C\,II}]_{158\ \mu\mathrm{m}}$ Line Emitters

In this appendix we present the candidate $[\mathrm{C\,II}]_{158\ \mu\mathrm{m}}$ line emitters recovered in our search detailed in Section 4 in Figure 16. For each source, we show the emission-line map and the two control maps velocity-integrated over $1.2\times$ the FWHM of the detected line in the $r = 2''$ aperture-integrated spectrum.

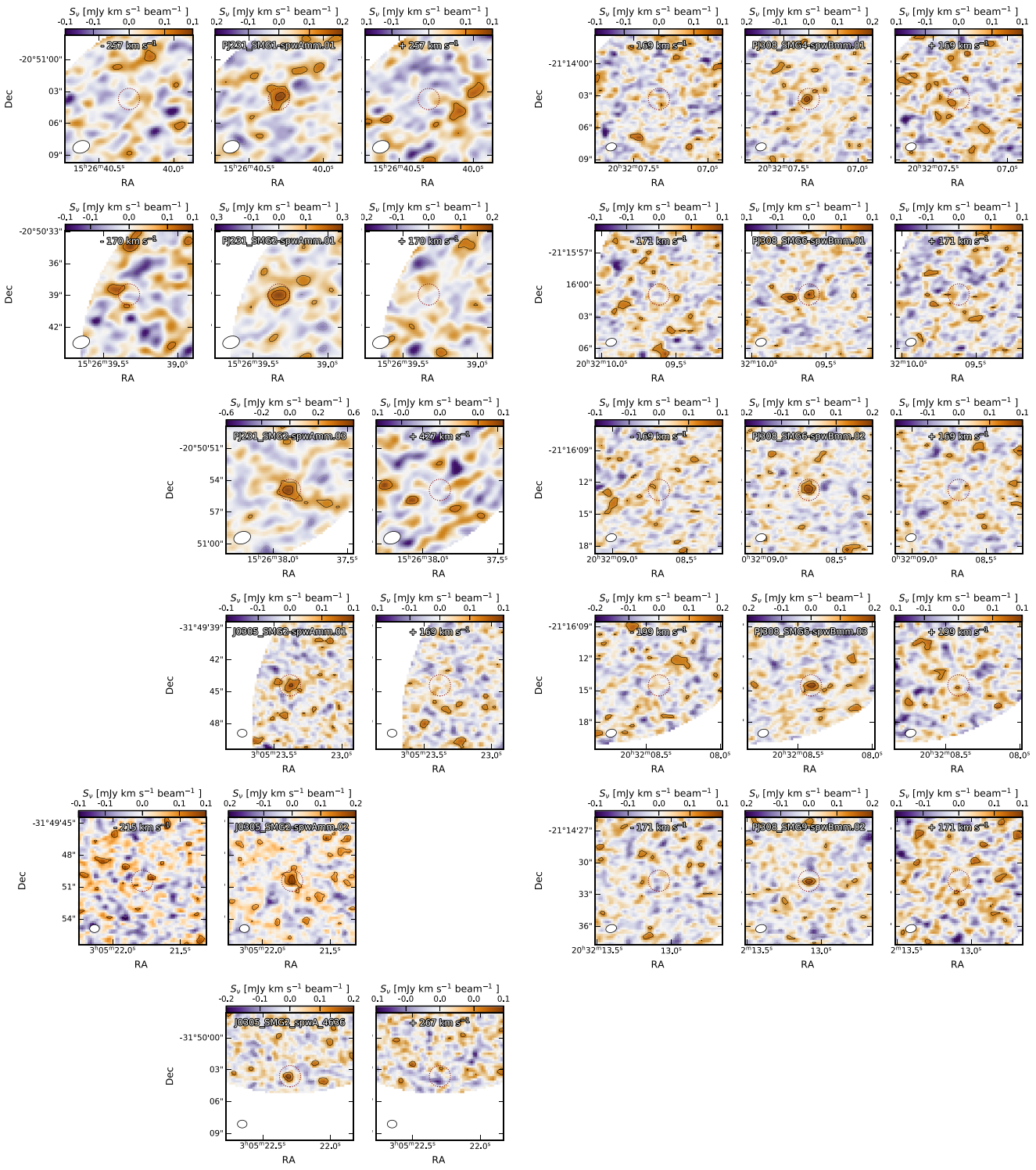

Figure 16. Emission-line maps for the secure line emitters (center, circled in dashed red) in the SMG fields. As in Figure 4, the emission-line maps are integrated over 1.2× FWHM of the fitted Gaussian profile to the spectra, and control maps with similar width but offset in velocity are provided in each case. The color scaling is log-linear for better contrast, and the contours are logarithmic: (−2, 2, 4, 8, 16, 32) σ, where σ is the rms noise (see Table 1). The beam is plotted in the lower left corner.

ORCID iDs

Romain A. Meyer https://orcid.org/0000-0001-5492-4522
Roberto Decarli https://orcid.org/0000-0002-2662-8803
Fabian Walter https://orcid.org/0000-0003-4793-7880
Qiong Li https://orcid.org/0000-0002-3119-9003
Ran Wang https://orcid.org/0000-0003-4956-5742
Chiara Mazzucchelli https://orcid.org/0000-0002-5941-5214
Eduardo Bañados https://orcid.org/0000-0002-2931-7824
Emanuele P. Farina https://orcid.org/0000-0002-6822-2254
Bram Venemans https://orcid.org/0000-0001-9024-8322

References

Ajiki, M., Taniguchi, Y., Murayama, T., et al. 2006, PASJ, 58, 499
Angulo, R. E., Springel, V., White, S. D. M., et al. 2012, MNRAS, 425, 2722
Bacon, R., Piqueras, L., Conseil, S., Richard, J., & Shepherd, M. 2016, MPDAF: MUSE Python Data Analysis Framework, Astrophysics Source Code Library, ascl:1611.003
Bañados, E., Venemans, B., Walter, F., et al. 2013, ApJ, 773, 178
Bañados, E., Venemans, B. P., Decarli, R., et al. 2016, ApJS, 227, 11
Bañados, E., Venemans, B. P., Mazzucchelli, C., et al. 2018, Natur, 553, 473
Barger, A. J., Wang, W. H., Cowie, L. L., et al. 2012, ApJ, 761, 89
Battisti, A. J., da Cunha, E., Grasha, K., et al. 2019, ApJ, 882, 61
Beelen, A., Cox, P., Benford, D. J., et al. 2006, ApJ, 642, 694
Begelman, M. C., Volonteri, M., & Rees, M. J. 2006, MNRAS, 370, 289
Bertin, E., & Arnouts, S. 1996, A&AS, 117, 393
Bond, J. R., Arnett, W. D., & Carr, B. J. 1984, ApJ, 280, 825
Boogaard, L., Meyer, R. A., & Novak, M. 2021, Interferopy: analysing datacubes from radio-to-submm observations, Zenodo, v1.0.0, doi:10.5281/zenodo.5775603
Bosman, S. E., Ďurovčíková, D., Davies, F. B., & Eilers, A. C. 2021, MNRAS, 503, 2077
Bosman, S. E. I., Kakiichi, K., Meyer, R. A., et al. 2020, ApJ, 896, 49
Bromm, V., & Loeb, A. 2003, ApJ, 596, 34
Carnall, A. C., Shanks, T., Chehade, B., et al. 2015, MNRAS, 451, L16
Champagne, J. B., Decarli, R., Casey, C. M., et al. 2018, ApJ, 867, 153
Chen, S.-F. S., Simcoe, R. A., Torrey, P., et al. 2017, ApJ, 850, 188
Da Cunha, E., Groves, B., Walter, F., et al. 2013, ApJ, 766, 13
Da Cunha, E., Walter, F., Smail, I. R., et al. 2015, ApJ, 806, 110
de La Vieuville, G., Bina, D., Pello, R., et al. 2019, A&A, 628, A3
De Rosa, G., Decarli, R., Walter, F., et al. 2011, ApJ, 739, 56
De Rosa, G., Venemans, B. P., Decarli, R., et al. 2014, ApJ, 790, 145
Decarli, R., Aravena, M., Boogaard, L., et al. 2020, ApJ, 902, 110
Decarli, R., Dotti, M., Bañados, E., et al. 2019, ApJ, 880, 157
Decarli, R., Walter, F., Venemans, B. P., et al. 2017, Natur, 545, 457
Decarli, R., Walter, F., Venemans, B. P., et al. 2018, ApJ, 854, 97
Devecchi, B., & Volonteri, M. 2009, ApJ, 694, 302
Díaz-Santos, T., Armus, L., Charmandaris, V., et al. 2017, ApJ, 846, 32
Drake, A. B., Farina, E. P., Neeleman, M., et al. 2019, ApJ, 881, 131
Drake, A. B., Garel, T., Wisotzki, L., et al. 2017, A&A, 608, A6
Dunne, L., Eales, S. A., & Edmunds, M. G. 2003, MNRAS, 341, 589
Eftekharzadeh, S., Myers, A. D., Hennawi, J. F., et al. 2017, MNRAS, 468, 77
Eftekharzadeh, S., Myers, A. D., & Kourkchi, E. 2019, MNRAS, 486, 274
Ester, M., Kriegel, H.-P., Sander, J., & Xu, X. 1996, in Proc. 2nd Int. Conf. on Knowledge Discovery and Data Mining 96 (Palo Alto, CA: AAAI), 226
Fan, X., Hennawi, J. F., Richards, G. T., et al. 2004, AJ, 128, 515
Fan, X., Narayanan, V. K., Lupton, R. H., et al. 2001, AJ, 122, 2833
Fan, X., Strauss, M. A., Becker, R. H., et al. 2006, AJ, 132, 117
Farina, E. P., Arrigoni-Battaia, F., Costa, T., et al. 2019, ApJ, 887, 196
Farina, E. P., Venemans, B. P., Decarli, R., et al. 2017, ApJ, 848, 78
Ferrara, A., Salvadori, S., Yue, B., & Schleicher, D. 2014, MNRAS, 443, 2410
García-Vergara, C., Hennawi, J. F., Barrientos, L. F., & Battaia, F. A. 2019, ApJ, 886, 79
García-Vergara, C., Hennawi, J. F., Felipe Barrientos, L., & Rix, H. W. 2017, ApJ, 848, 7
García-Vergara, C., Rybak, M., Hodge, J., et al. 2021, arXiv:2109.09754
Garel, T., Blaizot, J., Rosdahl, J., et al. 2021, MNRAS, 504, 1902
Gehrels, N. 1986, ApJ, 303, 336
González-López, J., Bauer, F. E., Romero-Cañizales, C., et al. 2017, A&A, 597, A41
González-López, J., Decarli, R., Pavesi, R., et al. 2019, ApJ, 882, 139
Goto, T., Utsumi, Y., Kikuta, S., et al. 2017, MNRAS, 470, L117
Gronke, M., Ocvirk, P., Mason, C., et al. 2021, MNRAS, 508, 3697
Habouzit, M., Volonteri, M., Somerville, R. S., et al. 2019, MNRAS, 489, 1206
Haiman, Z., & Quataert, E. 2004, in Supermassive Black Holes in the Distant Universe, ed. A. J. Barger (Dordrecht: Springer Netherlands), 147
Harris, C. R., Jarrod Millman, K., van der Walt, S. J., et al. 2020, Natur, 585, 357
Hennawi, J. F., Strauss, M. A., Oguri, M., et al. 2006, AJ, 131, 1
Herenz, E. C., & Wisotzki, L. 2017, A&A, 602, A111
Herrera-Camus, R., Sturm, E., Graciá-Carpio, J., et al. 2018, ApJ, 861, 95
Hodge, J. A., Karim, A., Smail, I., et al. 2013, ApJ, 768, 91
Holland, W. S., Bintley, D., Chapin, E. L., et al. 2013, MNRAS, 430, 2513
Hopkins, P. F., Hernquist, L., Cox, T. J., & Kereš, D. 2008, ApJS, 175, 356
Hu, E. M., Cowie, L. L., Songaila, A., et al. 2016, ApJ, 825, L7
Hunter, J. D. 2007, CSE, 9, 90
Hwang, H. S., Elbaz, D., Magdis, G., et al. 2010, MNRAS, 409, 75
Inayoshi, K., & Haiman, Z. 2014, MNRAS, 445, 1549
Inayoshi, K., Visbal, E., & Haiman, Z. 2020, ARA&A, 58, 27
Jiang, L., McGreer, I. D., Fan, X., et al. 2016, ApJ, 833, 222
Jorsater, S., & van Moorsel, G. A. 1995, AJ, 110, 2037
Katz, H., Sijacki, D., & Haehnelt, M. G. 2015, MNRAS, 451, 2352
Kayo, I., & Oguri, M. 2012, MNRAS, 424, 1363
Kim, S., Stiavelli, M., Trenti, M., et al. 2009, ApJ, 695, 809
Konno, A., Ouchi, M., Shibuya, T., et al. 2018, PASJ, 70, S16
Latif, M. A., & Ferrara, A. 2016, PASA, 33, 16
Latif, M. A., Schleicher, D. R. G., Schmidt, W., & Niemeyer, J. C. 2013, MNRAS, 436, 2989
Latif, M. A., & Volonteri, M. 2015, MNRAS, 452, 1026
Lee, J. C., Hwang, H. S., & Song, H. 2021, MNRAS, 503, 4309
Li, J., Wang, R., Cox, P., et al. 2020a, ApJ, 900, 131
Li, Q., Wang, R., Fan, X., et al. 2020b, ApJ, 900, 12
Lu, N., Zhao, Y., Díaz-Santos, T., et al. 2017, ApJS, 230, 1
Madau, P., Ferrara, A., & Rees, M. J. 2001, ApJ, 555, 92
Matthee, J., Sobral, D., Gronke, M., et al. 2018, A&A, 619, A136
Mazzucchelli, C., Bañados, E., Decarli, R., et al. 2017a, ApJ, 834, 83
Mazzucchelli, C., Bañados, E., Venemans, B. P., et al. 2017b, ApJ, 849, 91
Mazzucchelli, C., Decarli, R., Farina, E. P., et al. 2019, ApJ, 881, 163
Meyer, R. A., Kakiichi, K., Bosman, S. E. I., et al. 2020a, MNRAS, 494, 1560
Meyer, R. A., Laporte, N., Ellis, R. S., Verhamme, A., & Garel, T. 2020b, MNRAS, 500, 558
Mignoli, M., Gilli, R., Decarli, R., et al. 2020, A&A, 642, L1
Miller, T. B., Chapman, S. C., Hayward, C. C., et al. 2020, ApJ, 889, 98
Mortlock, D. J., Warren, S. J., Venemans, B. P., et al. 2011, Natur, 474, 616
Narayanan, D., Li, Y., Cox, T. J., et al. 2008, ApJS, 174, 13
Neeleman, M., Bañados, E., Walter, F., et al. 2019, ApJ, 882, 10
Neeleman, M., Novak, M., Venemans, B. P., et al. 2021, ApJ, 911, 141
Novak, M., Bañados, E., Decarli, R., et al. 2019, ApJ, 881, 63
Novak, M., Venemans, B. P., Walter, F., et al. 2020, ApJ, 904, 131
Oh, S. P., & Haiman, Z. 2002, ApJ, 569, 558
Oke, J. B., & Gunn, J. E. 1983, ApJ, 266, 713, (1983), 266, 713
Omukai, K., Schneider, R., & Haiman, Z. 2008, ApJ, 686, 801
Ouchi, M., Shimasaku, K., Furusawa, H., et al. 2010, ApJ, 723, 869
Overzier, R. A., Guo, Q., Kauffmann, G., et al. 2009, MNRAS, 394, 577
Paulino-Afonso, A., Sobral, D., Ribeiro, B., et al. 2018, MNRAS, 476, 5479
Peng, C. Y., Ho, L. C., Impey, C. D., & Rix, H.-W. 2002, AJ, 124, 266
Peng, C. Y., Ho, L. C., Impey, C. D., & Rix, H. W. 2010, AJ, 139, 2097
Pensabene, A., Decarli, R., Bañados, E., et al. 2021, A&A, 652, A66
Popping, G., Narayanan, D., Somerville, R. S., Faisst, A. L., & Krumholz, M. R. 2019, MNRAS, 482, 4906
Reed, S., McMahon, R. G., Banerji, M., et al. 2015, MNRAS, 454, 3952
Reed, S., McMahon, R. G., Martini, P., et al. 2017, MNRAS, 468, 4702
Sakurai, Y., Yoshida, N., Fujii, M. S., & Hirano, S. 2017, MNRAS, 472, 1677
Shen, Y., Strauss, M. A., Oguri, M., et al. 2007, AJ, 133, 2222
Simpson, C., Mortlock, D., Warren, S., et al. 2014, MNRAS, 442, 3454
Smolčić, V., Aravena, M., Navarrete, F., et al. 2012, A&A, 548, A4
Sobral, D., Santos, S., Matthee, J., et al. 2018, MNRAS, 476, 4725
Songaila, A., Hu, E. M., Barger, A. J., et al. 2018, ApJ, 859, 91
Soto, K. T., Lilly, S. J., Bacon, R., Richard, J., & Conseil, S. 2016, MNRAS, 458, 3210
The Astropy Collaboration, Price-Whelan, A. M., Sipőcz, B. M., et al. 2018, AJ, 156, 19
Utsumi, Y., Goto, T., Kashikawa, N., et al. 2010, ApJ, 721, 1680
Uzgil, B. D., Oesch, P. A., Walter, F., et al. 2021, ApJ, 912, 67
Valiante, R., Schneider, R., Volonteri, M., & Omukai, K. 2016, MNRAS, 457, 3356
Venemans, B., Neeleman, M., Walter, F., et al. 2019, ApJL, 874, L30
Venemans, B. P., Bañados, E., Decarli, R., et al. 2015, ApJL, 801, L11
Venemans, B. P., Findlay, J. R., Sutherland, W. J., et al. 2013, ApJ, 779, 24
Venemans, B. P., McMahon, R. G., Warren, S. J., et al. 2007, MNRAS, 376, L76
Venemans, B. P., Walter, F., Neeleman, M., et al. 2020, ApJ, 904, 130
Venemans, B. P., Walter, F., Zschaechner, L., et al. 2016, ApJ, 816, 37
Verhamme, A., Garel, T., Ventou, E., et al. 2018, MNRAS, 478, L60
Virtanen, P., Gommers, R., Oliphant, T. E., et al. 2020, NatMe, 17, 261
Volonteri, M. 2010, A&ARv, 18, 279
Walter, F., & Brinks, E. 1999, AJ, 118, 273
Walter, F., Brinks, E., de Blok, W. J. G., et al. 2008, AJ, 136, 2563

Walter, F., Decarli, R., Aravena, M., et al. 2016, ApJ, 833, 67
Wang, F., Yang, J., Fan, X., et al. 2018, ApJ, 869, L9
Wang, F., Yang, J., Fan, X., et al. 2021, ApJL, 907, L1
Willott, C. J., Bergeron, J., & Omont, A. 2017, ApJ, 850, 108
Willott, C. J., Percival, W. J., McLure, R. J., et al. 2005, ApJ, 626, 657
Wise, J. H., Regan, J. A., O'Shea, B. W., et al. 2019, Natur, 566, 85
Yang, J., Wang, F., Fan, X., et al. 2019, AJ, 157, 236
Yang, J., Wang, F., Fan, X., et al. 2020, ApJ, 897, L14